Strontium Calcium Phosphate Nanotubes as Bioinspired Building Blocks for Bone Regeneration — Source link ⤢

Camila B. Tovani, Tamires M. Oliveira, Mariana P. R. Soares, Nadine Nassif ...+4 more authors

Institutions: Faculdade de Filosofia, Ciências e Letras de Ribeirão Preto, University of São Paulo, Collège de France, Université Paris-Saclay

Topics: Bone regeneration and Biomineralization

Related papers:

- Fabrication of collagen membranes with different intrafibrillar mineralization degree as a potential use for GBR.

- Phosphorylated chitosan to promote biomimetic mineralization of type I collagen as a strategy for dentin repair and bone tissue engineering

- Alginate-Assisted Mineralization of Collagen by Collagen Reconstitution and Calcium Phosphate Formation.

- Conversion of functions by nanosizing—from osteoconductivity to bone substitutional properties in apatite

- Biomimetic mineralization of recombinant collagen type I derived protein to obtain hybrid matrices for bone regeneration.

Strontium Calcium Phosphate Nanotubes as Bioinspired Building Blocks for Bone Regeneration

Camila Tovani, Tamires Oliveira, Mariana Soares, Nadine Nassif, Sandra Fukada, Pietro Ciancaglini, Alexandre Gloter, Ana Ramos

Biological and Medical Applications of Materials and Interfaces

Strontium-calcium phosphate nanotubes as bioinspired building blocks for bone regeneration

Camila B. Tovani, Tamires Maira Oliveira, Mariana P R Soares, Nadine Nassif,
Sandra Yasuyo Fukada, Pietro Ciancaglini, Alexandre Gloter, and Ana Paula Ramos

Strontium-calcium phosphate nanotubes as bioinspired building blocks for bone regeneration

Camila B. Tovani[1], Tamires M. Oliveira[1], Mariana P. R. Soares[2], Nadine Nassif[3], Sandra Y. Fukada[2], Pietro Ciancaglini[1], Alexandre Gloter[4], Ana P. Ramos[1]*

1. Departamento de Química, Faculdade de Filosofia, Ciências e Letras de Ribeirão Preto, Universidade de São Paulo, Ribeirão Preto, SP, Brazil

2. Departamento de Ciências Biomoleculares, Faculdade de Ciências Farmacêuticas de Ribeirão Preto, Universidade de São Paulo, Ribeirão Preto, SP, Brazil

3. Sorbonne Université, CNRS, Collège de France, Laboratoire de Chimie de la Matière Condensée de Paris, 4 Place Jussieu, F-75005 Paris, France

4. Laboratoire de Physique des Solides, Université Paris-Saclay, 91405 Orsay, France

*Corresponding author- e-mail: anapr@ffclrp.usp.br

Keywords: biomineralization, calcium phosphate, strontium, collagen, confinement, nanotubes

1   **Abstract**

2   Calcium phosphates (CaPs) based ceramics are the most investigated materials for bone

3   repairing and regeneration. However, the clinical performance of commercial ceramics

4   is still far from that of the native tissue which remains as the gold standard. Thus,

5   reproducing the structural architecture and composition of bone matrix should trigger

6   biomimetic response in synthetic materials. Here, we propose an innovative strategy

7   based on the use of track-etched membranes as physical confinement to produce

8   collagen-free strontium substituted-CaPs nanotubes that tend to mimic the building

9   block of bone, *i.e.* the mineralized collagen fibrils. A combination of high-resolution

10 microscopic and spectroscopic techniques revealed the underlying mechanisms driving

11 the nanotubes formation. Under confinement poorly crystalline apatite platelets

12 assembled into tubes which resembled the mineralized collagen fibrils in terms of

13 diameter and structure of bioapatite. Furthermore, the synergetic effect of Sr^{2+} and

14 confinement gave rise to the stabilization of amorphous strontium-CaPs nanotubes. The

15 nanotubes were tested in long-term culture of osteoblasts supporting their maturation

16 and mineralization without eliciting any cytotoxicity. The Sr^{2+} released from the

17 particles reduced the differentiation and activity of osteoclasts in a Sr^{2+}-concentration

18 dependent manner. Their bioactivity was evaluated in a serum-like solution showing

19 that the particles guided spatially the biomimetic remineralization. Further, these effects

20 were achieved at strikingly low concentrations of Sr^{2+} that is crucial to avoid side

21 effects. Overall, these results open simple and promising pathways to develop a new

22 generation of CaPs multifunctional ceramics active in tissue regeneration and able to

23 simultaneously induce biomimetic remineralization and control the imbalanced

24 osteoclast activity responsible for bone-density loss.

1

1. INTRODUCTION

3

Producing materials able to conduct the cascade of events involved in tissue regeneration is an ongoing goal in biomaterials science. This requires reproducing the chemistry and structure of the native tissue.[1] In bone, the key mechanical and biological features arise mainly from the fibrillar pattern of the extracellular matrix.[2] Collagen molecules self-assemble into fibrils of 100-200 nm that are mineralized by apatite platelets providing a typical anisotropic environment that directs cell proliferation and differentiation.[3] Bone mineral contributes not only for the mechanical properties of the tissue but also supports its remodeling process and biochemical function of ionic reservoir.[4] This is ascribed to the low degree of crystallinity and the presence of amorphous domains that provides adequate resorption rate. Calcium phosphates (CaPs), are among the most extensively materials used to repair hard tissues injuries thanks to their chemical resemblance to the mineral phase of bone and teeth, suitable biocompatibility and low cost.[5] However, producing biomimetic CaPs particles remains challenging. In contrast to bone mineral, CaPs based commercial ceramics are usually stoichiometric and highly crystalline rendering poor osteogenic functions as compared to biological graft.[6] Consequently, rather than regenerative materials, the applications of CaPs are reduced to biologically passive replacers or fillers. Tuning the physicochemical properties is therefore crucial to trigger biomimetic response in synthetic materials.

To date, several strategies have been proposed to produce bioactive ceramics dedicated to bone regeneration, being the combination of CaPs with collagen regarded as one of the most effective approach to mimic the fibrillar nature of the tissue.[7,8] However, working with collagen is hard to handle and expensive. Additionally, (i)

1 denaturation of collagen molecule is easily induced *in vitro* compromising its ability to

2 self-assemble into fibrils and consequently the biocompatibility of the materials and (ii)

3 reaching fibrils monodisperse in size is not straightforward and requires high

4 concentrated collagen solutions which stabilization is challenging. One dimensional

5 particles with tunable diameter offer an alternative pathway to mimic the mineralized

6 collagen fibrils of bone. Apatite nano/micro tubes have been synthesized through

7 several conditions including hydrothermal routes, high temperatures and addition of

8 stabilizing agents.[9] Considerable progress has been made, however simultaneously

9 reproducing the structural features of bone mineral and the morphology of collagen

10 fibrils is still challenging and no CaPs particles which resemble the environment of

11 bone extracellular matrix have been achieved without the need of an organic scaffold.

12 Although biomimetic CaPs can repair damages, induce remineralization and

13 osteogenesis, they are not able to regulate the increased osteoclastic activity responsible

14 for osteoporosis.[10,11] In this sense, in addition to tune the structure and morphology, the

15 incorporation of Sr^{2+} in bioceramics represents a leap forward in the field of bone

16 regeneration.[12] Unlike the traditional osteoporosis therapies, Sr^{2+} exerts a twofold effect

17 on bone cells stimulating osteoblasts activity and decreasing osteoclasts metabolism

18 simultaneously, as desirable for treating and preventing osteoporosis.[13] Among the

19 materials investigated to locally deliver Sr^{2+}, amorphous CaPs stand out. It is readily

20 degraded by osteoclasts in the acidic environment during bone remodeling yielding both

21 ionic precursors to remineralization and Sr^{2+} to regulate the imbalanced cellular

22 activity.[14,15] The use of amorphous CaPs for bone repairing is especially advantageous

23 since they easily induce biomimetic remineralization.[10] Besides the encouraging clinical

24 results, one should emphasize that the side effects of Sr^{2+} cannot be neglected; its

25 accumulation in the tissue leads to pathological mineralization such as rickets and

4

1   1   osteomalacia.[16–18] Therefore, developing biomaterials able to reduce osteoclasts activity
2
3   2   at low doses of Sr^{2+} is of paramount significance since elderly people who may present
4
5   3   decreased renal function are the main target of osteoporosis treatments.
6
7
8   4   Here, we propose an innovative strategy based on the use of physical
9
10   5   confinement to produce collagen-free CaP nanotubes which tend to mimic the building
11
12   6   block of bone, the mineralized collagen fibrils. Under confinement, poorly crystalline
13
14
15   7   apatite platelets assembled into tubes, which simultaneously resemble both the fibrils
16
17   8   present in the extracellular matrix of bone in terms of diameter range and the structure
18
19
20   9   of bioapatite. Although collagen is described to define the structural features of bone
21
22   10   mineral, biomimetic apatite was formed here only by using physical confinement,
23
24   11   discarding the use of fibrillar polymers. The incorporation of Sr^{2+} changed the mineral
25
26   12   phase from apatite to amorphous CaP and strontium apatite. The Sr^{2+} released from the
27
28   13   particles in the cell culture medium increased alkaline phosphatase activity of
29
30   14   osteoblasts and decreased osteoclasts differentiation and resorption in a Sr^{2+}
31
32   15   concentration dependent manner. Notably, these effects were reached at extremely low
33
34
35   16   amounts of Sr^{2+} as compared to typical therapies based on strontium ranelate and
36
37   17   currently reported biomaterials.[19–21] The ability of the particles to promote biomimetic
38
39   18   remineralization was demonstrated by the deposition of bone-like apatite on their
40
41
42   19   surface after immersion in a simulated body fluid (SBF). These results evidence that the
43
44   20   particles synthesized herein open perspectives for new ceramics towards bone
45
46   21   regeneration.

1

2. EXPERIMENTAL PROCEDURE

2.1 Formation of strontium calcium phosphate Sr(CaP) nanotubes in physical confinement

Bioinspired precipitation of CaPs containing different amounts of Sr^{2+} (Sr(CaP)) was carried out in confined environment provided by the 200 nm cylindrical pores of commercial hydrophilic polycarbonate track-etched membranes (Millipore®) of 20 μm thickness, by modifying an approach described elsewhere.[22] The size of pores was chosen based on the diameter of collagen fibrils in bone. Briefly, (0.1 wt.% poly(acrylic acid) (PAA, Sigma MW1800 g mol^{-1}) was dissolved in aqueous solutions containing 0.006 mol L^{-1} H_3PO_4 (Sigma), $CaCl_2$ (Merck P.A.), $SrCl_2$ (Synth P.A.), or a mixture of these salts at different Sr^{2+} molar percentages (0, 10, 50, and 100%) in relation to the total number of mols of divalent cations ($Ca^{2+} + Sr^{2+}$). The total $[Ca^{2+}] + [Sr^{2+}]$ concentration was 0.01 mol L^{-1}. The (Ca + Sr)/P molar ratio was kept constant and equal to 1.67 and initial pH = 3.5. The membranes were initially plasma cleaned (Harrick-plasma chamber) using $N_2(g)$ for 2 min. In the sequence, they were immersed into the PAA/salt solution for 12 h allowing the penetration of the solution within the pores of the membrane. PAA is described to increase the synthesis yield by promoting the formation of the so-called mineral precursor phase PILP (polymer induced liquid precursor phase) which displays the liquid ability to infiltrate within restricted volumes by capillary action enhancing significantly the intra-membrane *versus* bulk precipitation.[23] The membranes were subsequently placed between two glass slides and put into a desiccator containing $(NH_4)_2CO_3$ at room temperature for 12h, as schematically represented in Figure 1. The $(NH_4)_2CO_3$ decomposition generates $CO_2(g)$ and $NH_3(g)$ that diffuse into the aqueous solutions increasing the pH which triggers the

1   mineral precipitation within the pores of the membrane. After precipitation, the surface

2   of the membranes was scraped using filter paper to remove particles that were not

3   formed within the pores. To recover the nanotubes, the membranes were dissolved with

4   chloroform followed by centrifugation (11000 rpm) three times. The particles were then

5   rinsed with ethanol and characterized.

6

7   **2.2 Precipitation from the bulk**

8   Precipitation from bulk solution was carried out as control experiments. To this

9   end, 50-mL flasks containing 20 mL of the PAA/salt starting solutions were placed in a

10   closed desiccator under identical reaction conditions used for the intramembrane

11   precipitation, *i.e.* precursors concentration, temperature, dissector volume and reaction

12   time. The precipitates were centrifugated, rinsed with ethanol and dried at room

13   temperature.

14
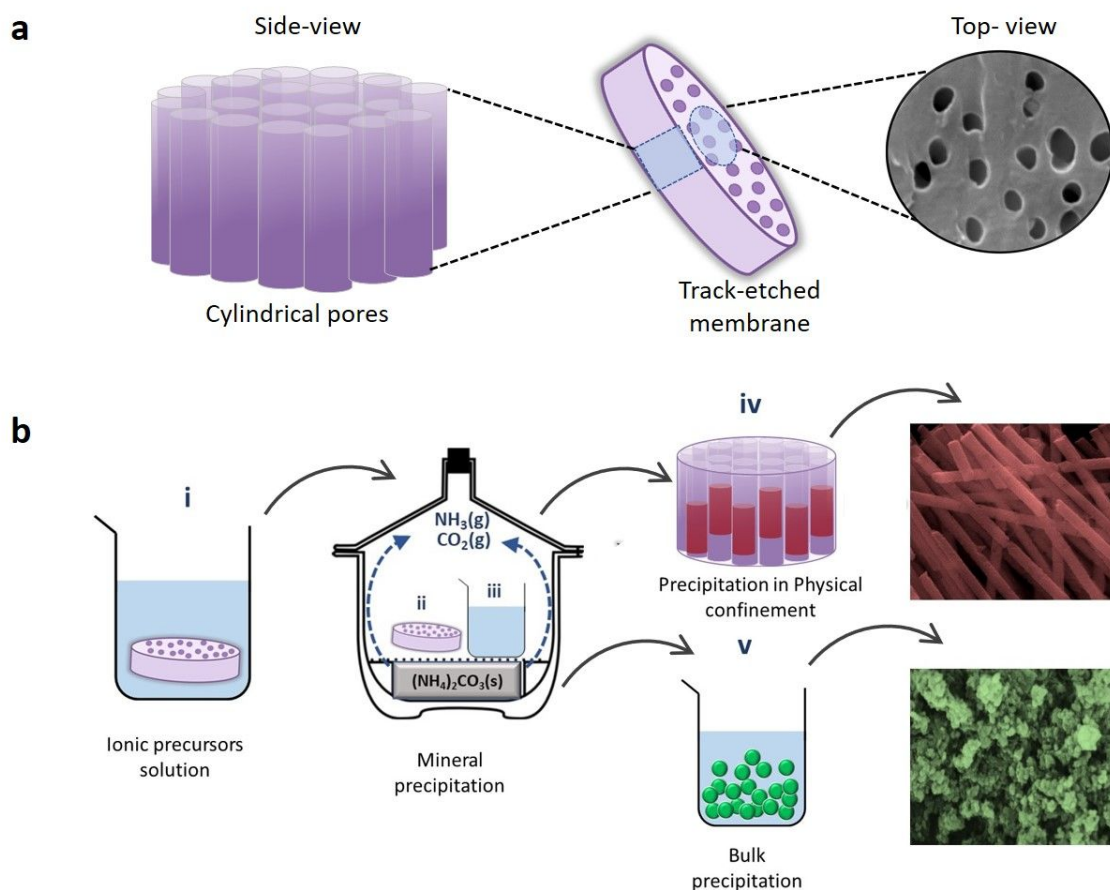
Figure 1. (a) Schematic representation of a track-etched membrane used as physical confinement to tune the morphology and size of the nanotubes. The side and top view of the membrane show the cylindrical pores where the precipitation takes place. A SEM image of the surface of a membrane shows the pores. (b) Schematic representation of the precipitation of Sr(CaP) under either physical confinement (i, ii, iv) or in bulk solution (iii and v). The membranes were immersed into the PAA/salt solution for 12 h (i) and then placed in a desiccator containing $(NH_4)_2CO_3$ (ii) leading to the formation of nanotubes inside the cylindrical pores (iv). The particles (reddish SEM image) were isolated by dissolving the membranes with chloroform followed by centrifugation. A beaker containing the PAA/salt solutions was placed in the desiccator (iii) to conduct the precipitation from bulk solution (v) leading to agglomerated spherical particles (greenish SEM image).

1

2.3 Ability of the particles to induce biomimetic mineralization *in vitro*

The particles were dispersed in simulated body fluid (SBF) at 37°C for 5 days to evaluate their ability to induce biomimetic precipitation of apatite in physiological environment. The procedure used to prepare SBF followed the International Standard Organization (ISO 23317) and is described elsewhere.[24] Briefly, 2.5 mmol L^{-1} Ca^{2+}, 142 mmol L^{-1} Na^+, 4.2 mmol L^{-1} HCO_3^-, 5 mmol L^{-1} K^+, 1.5 mmol L^{-1} Mg^{2+}, 147.8 mmol L^{-1} Cl^-, 1 mmol L^{-1} HPO_4^{2-} and 0.5 mmol L^{-1} SO_4^{2-} were dissolved in ultrapure water. The pH was adjusted to 7.4 with 11 mol L^{-1} tris-hydroxymethyl amine methane (Tris) and 1 mol L^{-1} HCl aqueous solution.[24]

2.4 Characterization of the samples

The morphology of the gold-coated particles was investigated by scanning electron microscopy (SEM) using a Zeiss-EVO 50 microscope under 20 kV accelerating voltage. For transmission electron microscopy (TEM) analysis, the samples were dispersed in ethanol and some drops were deposited on a lacey carbon film on copper grid. Energy dispersive spectroscopy (EDS) mapping of Ca, Sr and P was obtained on a single particle using a HRTEM microscope FEI TECNAI G2 F20 operating at 200 kV. TEM images and single particle selected area electron diffraction (SAED) patterns were acquired using a TEM microscope JEOL 2011 operating at 100 kV. Energy electron loss spectra (EELS) and scanning transmission electron microscope images (STEM) were acquired in a Nion STEM microscope at 200 keV. The chemical groups were identified by Fourier-transform infrared spectroscopy (FTIR) coupled with an attenuated total reflectance (ATR) accessory (Shimadzu-IRPrestige-21), with a resolution of 2 cm^{-1}. The X-ray diffraction patterns were acquired with a Bruker-AXS

1   D5005 diffractometer using Cu-K$_\alpha$ radiation at 40 kV and 30 mA. The diffraction peaks

2   were indexed based on the databank of the Joint Committee on Powder Diffraction. The

3   electrophoretic mobility measurements for the determination of zeta-potential (ζ) were

4   carried out in a Zetasizer Nano ZS (Malvern Instruments). For evaluation of ζ as a

5   function of the pH, 1 mg mL^{-1} of particles was dispersed in 0.001 mol L^{-1} NaCl

6   aqueous solution to keep constant the ionic strength. The pH was adjusted using 1 mol

7   L^{-1} HCl and 1 mol L^{-1} NaOH. ζ *versus* pH curves were also obtained to investigate the

8   behavior of the particles in the cell culture medium. To this end, the particles were

9   incubated with minimum essential medium (α-MEM, Gibco) supplemented with 10

10   wt.% fetal bovine serum for 30 min. In the sequence the particles were centrifugated

11   and gently washed with deionized water followed by redispersion in 0.001 mol L^{-1}

12   NaCl aqueous solution.

13

14   **2.5 Release of Sr^{2+}**

15   The Sr^{2+} released from the particles after immersion in cell culture medium for 1,

16   3, 7, 14 and 21 days was quantified by atomic absorption spectrometry with atomization

17   by acetylene-air flame in the equipment ContrAA 700 (Analytik Jena AG, Jena,

18   Germany). The samples were supplemented with La^{3+}

19   (10 g L^{-1}) and K^{+} (1 g L^{-1}) and the absorbance read at 460 and 733 nm.

20

21   **2.6 Cellular response *in vitro***

22   *2.6.1 MC3T3-E1 viability and mineralization ability*

23   Osteoblastic lineage cells MC3T3-E1 (American Type Culture Collection-

24   ATCC) were cultured in α-MEM (Gibco) supplemented with 10 wt.% fetal bovine

25   serum and 1 vol.% penicillin/streptomycin. This is a lineage with an osteoblastic

1   phenotype that undergoes a proliferation–differentiation sequence, leading to the

2   mineralization of bone-like extracellular matrix. The osteogenic medium was achieved

3   by the addition of ascorbic acid and β-glycerophosphate. Briefly, the cells were seeded

4   on 24-well plates at the density of 2.10^4 cells per well and incubated in air at 37 ºC and

5   5% CO_2. The plated cells were then allowed to attach to the polystyrene well bottoms

6   for   24h,   followed   by   the   replacement   of   the   medium   for   a

7    $1\mu g\ mL^{-1}$ suspension of nanotubes (0% Sr^{2+}, 10% Sr^{2+}, 50% Sr^{2+} and 100% Sr^{2+}) in the

8   culture medium. The medium was changed every two days keeping constant the

9   concentration of the particles. Cell viability was determined by MTT (3(4,5-dimethyl-

10   thiazole-2-yl)2,5-diphenyl tetrazolium bromide, Sigma-Aldrich) assay after 7, 14 and 21

11   days of culture using the protocol described by Mosmann.[25] Cell viability was expressed

12   as the percentage of the average of 3 experiments as compared to the control (Ct)

13   without treatment, for each day of culture (100%). ALP activity was determined by

14   quantifying the hydrolysis of the substrate p-nitrophenyl phosphate (PNPP, Sigma-

15   Aldrich) in the plasma membrane fraction extracted from cells after 7 and 14 days of

16   culture, according to the protocol described elsewhere.[26] The enzymatic activity was

17   normalized by the total protein content which was estimated by the Hartree

18   methodology, in the presence of 2 wt.% sodium dodecyl sulfate and using bovine serum

19   albumin as standard.[27] To this end, the absorbance of the samples was read at 650 nm

20   with a spectrometer. After culturing for 21 days, the formation of the mineralized

21   extracellular matrix was investigated by Alizarin Red S (Sigma-Aldrich) staining

22   according to the methodology described elsewhere.[28] To avoid the interference of

23   Sr(CaP) particles, the wells were first gently washed with phosphate saline buffer (three

24   times) removing possible loosely-bounded precipitates from the culture medium. In the

25   sequence, the samples were fixed in 1.5 vol.% glutaraldehyde at 4 ºC for 12 h and

1 dehydrated through a series of ethanol concentrations (30, 50, 70, and 100 vol.%). The

2 content of the wells was solubilized in acetic acid and neutralized with ammonium

3 hydroxide. The formation of mineral nodules was then followed by reading the

4 absorbance of the samples at 405 nm.

5

6 *2.6.2 Cell morphology*

7   SEM was applied to investigate morphology of cells. The cells cultured on the

8 polystyrene discs were fixed in 1.5 vol% glutaraldehyde at 4 ºC for 12 h, and

9 dehydrated through a series of ethanol concentrations (20, 50, 70, 80, 90 and 100

10 vol.%), dried using supercritical CO_2 conditions and contrasted with OsO_4. After coated

11 with gold, the samples were observed on a Zeiss-EVO 50 SEM microscope under 20 kV

12 accelerating voltage. The morphology of attached cells was also investigated by

13 confocal microscopy. For this, after the fixation step, the samples were stained with 5

14 µg mL^{-1} acridine orange (Sigma-Aldrich) and then visualized using a confocal laser

15 scanning microscope (Leica TCS SP5). This fluorophore binds to the osteoblast nucleic

16 acids providing a contrasted image. To visualize DNA, the sample was excited with the

17 488 nm line of an argon laser, and emission was collected between 499 and 541 nm

18 (green). RNA was visualized by exciting the sample with the 458 nm line of an argon

19 laser, and emission was collected between 642 and 682 nm (red).

20 *2.6.3 Osteoclasts differentiation and resorption activity*

21   Bone marrow macrophages (BMMs) were isolated from long bone of 6- to 8-

22 wk-old C57BL/6 mice and were cultured in α-MEM (GIBCO, Invitrogen) supplemented

23 with 10 wt.% fetal bovine serum (FBS; Sigma-Aldrich), 1 vol.% penicillin-

24 streptomycin, and 30 ng mL^{-1} M-CSF (R&D Systems). After 3 days, adherents BMMs

25 were collected, seeded at a density of 2.10^4 cells/well in 96-well plates or

12

1   hydroxyapatite-coated plates. Cells were cultured for 2 days in osteoclastogenic

2   medium condition: M-CSF (30 ng mL^{-1}) and RANKL (10 ng mL^{-1}). Then, the

3   osteoclastogenic medium was replaced by 1 μg mL^{-1} dispersion of the of Sr(CaP)

4   nanotubes containing 0, 10, 50, 100 mol% Sr^{2+} in the culture medium. Osteoclast-

5   differentiated cells on day 4 were confirmed by tartrate-resistant acid phosphatase

6   (TRAP) staining (Sigma-Aldrich 387A kit). The osteoclast number (TRAP-positive

7   cells containing 3 or more nuclei) was analyzed in 5 wells per group using ImageJ

8   software (National Institutes of Health). Resorption area was measured in

9   hydroxyapatite-coated 96 well plate (OsteoAssay-Corning) on day 5 of culture. The

10 results were representative of two independent experiments.

1

2 3. RESULTS AND DISCUSSION

3 **3.1 Synthesis of Sr(CaP) nanotubes: effect of physical confinement and Sr^{2+}**
4 **concentration**

5

6   The effects of the physical confinement in the precipitation of Sr(CaP) particles

7 were distinguished by comparison with control experiments in which the precipitation

8 was carried out in bulk solution. SEM images of the polycarbonate track-etched

9 membranes used as physical confinement are shown in Figure S1. The effect of Sr^{2+}

10 concentration was also investigated. Polydisperse and agglomerated spherical particles

11 formed in the control experiments (Figure 2a). The spherical morphology is typical of

12 apatite grown in the presence of high concentration of CO_3^{2-}.[29] Well defined tubes

13 formed within the pores of polycarbonate membranes regardless the amount of Sr^{2+},

14 confirming the role of physical confinement in defining the particles diameter and

15 morphology (Figure 2b). Notably, these particles resemble the collagen fibrils found in

16 the extracellular matrix of bone in terms of diameter range and mineral interface.[30] To

17 demonstrate the versatility of this approach to control the morphology and size of the

18 particles, Sr(CaP) tubes with 400 nm diameter were synthesized using polycarbonate

19 membranes with 400 nm pores (Figure S2). The Sr^{2+} incorporation in the solids was

20 proportional to its concentration in the starting solutions regardless the use of

21 confinement, as determined by TEM-EDS (Table S1).

22   The mineral composition of the spherical particles precipitated in bulk solution

23 and tubes precipitated under confinement was investigated by XRD (Figures 2c and 2d,

24 respectively). In the absence of Sr^{2+} (0% Sr^{2+}) apatite was formed in the control together

25 with other CaPs (indicated by * in the diffractogram). Although some peaks could be

26 identified as octacalcium phosphate (OCP) the low amount of material precluded the

1 complete identification of these additional phases by XRD. Poorly crystalline apatite

2 resembling bone mineral was selectively formed within the membrane pores at 0%

3 Sr^{2+}.[31] The addition of 10% Sr^{2+} in the control lead to strain in the crystalline structure

4 of apatite as suggested by the broader diffraction peaks (Figure 2c). Moreover, the shift

5 of the 002 peak towards lower values of 2θ supports the Ca^{2+} replacement by Sr^{2+} in the

6 apatite lattice. At the same 10% Sr^{2+}, amorphous strontium calcium phosphate Sr(ACP)

7 was formed under confinement (Figure 2d). At 50% Sr^{2+}, Sr(ACP) was precipitated in

8 the control as indicated by the characteristic humps at 2θ close to 30º (Figure 2c), in

9 agreement with previous investigations.[32] Additionally, some peaks assigned to

10 strontianite ($SrCO_3$, indicated by S in the diffractogram) were also detected.[33] This was

11 expected as the critical pH for the mineral precipitation was triggered by the

12 decomposition of $(NH_4)_2CO_3$. In contrast, diffraction peaks were not observed for the

13 samples containing 50% Sr^{2+} precipitated within the membrane´s pores, showing that

14 confinement promotes the amorphization of both phosphate and carbonate. This

15 indicates therefore that this sample is formed by a mixture of Sr(ACP) and amorphous

16 strontium calcium carbonate Sr(ACC). Increased amount of Sr^{2+} up to 100% resulted in

17 the precipitation of strontium hydrogen phosphate for the control, while strontium

18 apatite was formed under confinement. Table S2 summarizes the products obtained in

19 bulk solution and in confinement. ζ results evidenced the structural changes described

20 by XRD due to the incorporation of Sr^{2+} in the particles (Figure S3). ATR-FTIR spectra

21 confirmed that, likewise the mineral found in the bone tissue and tooth enamel, the

22 nanotubes are made of carbonated apatite, thus strengthening their biomimetic nature

23 (Figure S4).[34] This is an important feature considering the application of these particles

24 as building blocks for bone regeneration.

25

1

2

Figure 2. SEM images of the phosphate particles formed in bulk solution (a) and in confinement (b). XRD pattern of the particles synthesized in bulk solution (c) and in confinement (d). The products formed in bulk solution were indexed as follows: hydroxyapatite for 0% Sr^{2+} and 10% Sr^{2+} (JCPDS 9-432). The additional peaks (*) observed in the 0% Sr^{2+} sample may be due to OCP (JPDCS 26–1056). Strontianite (S) (JPDCS 01-071-4899) was found in the 50% Sr^{2+} sample in addition to an amorphous phase Sr(ACP). Strontium hydrogen phosphate was identified in the 100% Sr^{2+} sample (JCPDS 23-105026). The samples formed in confinement were identified as hydroxyapatite (0% Sr^{2+}), Sr(ACP) (10% Sr^{2+} and 50% Sr^{2+}) and strontium hydroxyapatite (100% Sr^{2+}) (JPDCS 33-1348).

1

2   The tubes formed under physical confinement were further characterized by

3   TEM-BF (bright field), STEM-HAADF (high angle annular dark field) microscopy and

4   SAED (Figure 3). As expected, the tubes display a diameter of 200 nm. The samples

5   containing 0, 10 and 50% Sr^{2+} displayed a hollow structure which characterized them as

6   tubes. This was unambiguous from the STEM-HAADF images that were sensitive to

7   the amount of projected materials with higher thickness appearing brighter.

8   Furthermore, vase-like structures were observed suggesting that the precipitation started

9   at the bottom of the membrane and progressed along the pore leading to narrowing tube

10   walls (Figure S5). In the absence of Sr^{2+}, the tubes were polycrystalline composed of

11   nanometric platelets resembling the morphology of apatite in bone. Their apatite

12   structure was confirmed by the typical SAED patterns.

13   The absence of crystalline reflections in the SAED patterns of the 10% Sr^{2+} and

14   50% Sr^{2+} tubes confirms their amorphous character depicted by XRD. The 100% Sr^{2+}

15   rods were polycrystalline, with grain sizes of several tens of nm and unlike the Ca^{2+}-

16   bearing particles they were not hollow. Elementary EDS-TEM mapping results show

17   that the elements Ca, Sr, P, and O were homogeneously distributed within the Sr(ACP)

18   particles, at least with the resolution of the EDS system (Figure S6).

17
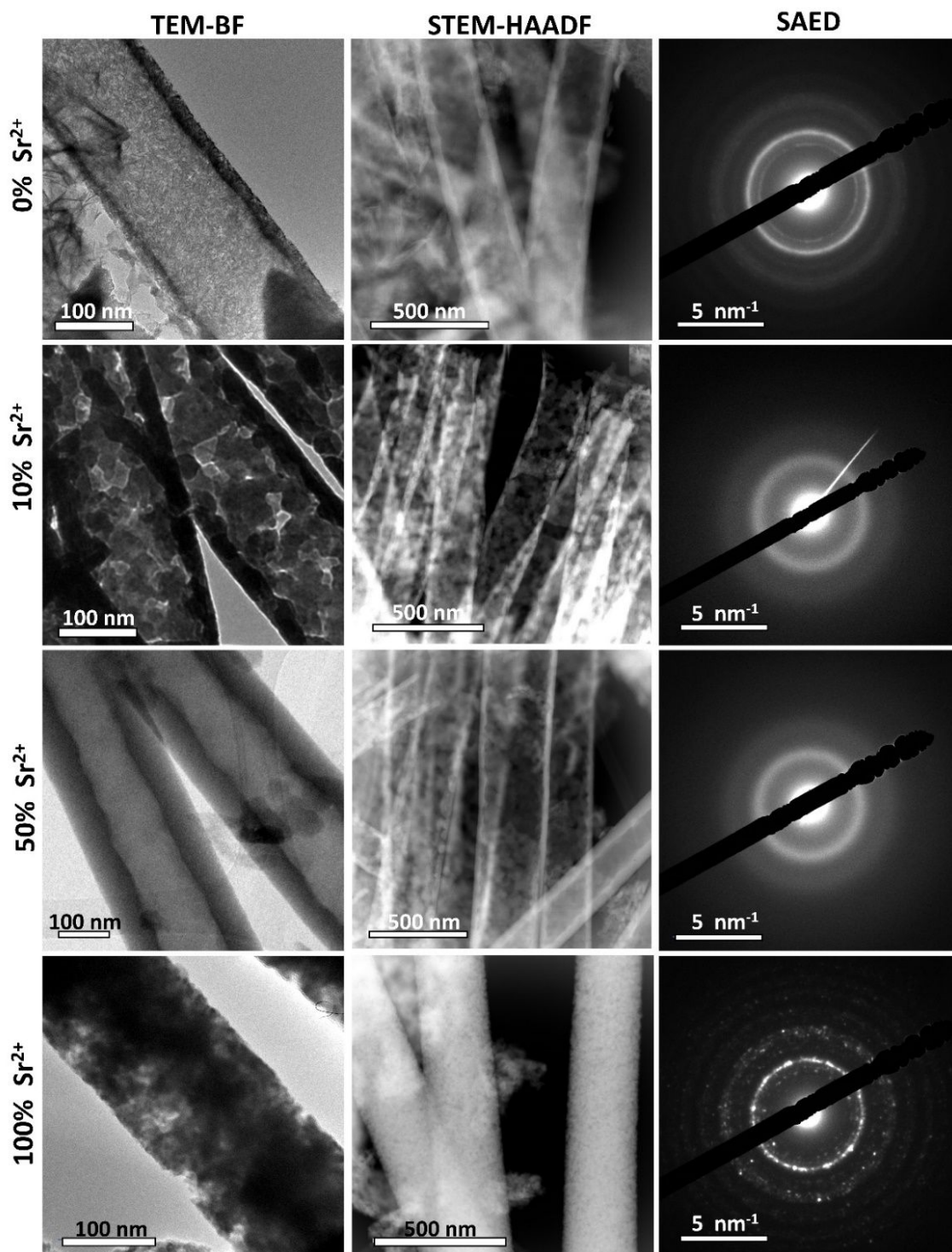
Figure 3.TEM-BF, STEM-HAADF images and SAED patterns of the 0, 10, 50, and 100% Sr^{2+} nanotubes. STEM-HAADF images show that the 0% Sr^{2+}, 10% Sr^{2+} and 50% Sr^{2+} nanotubes are hollow. The absence of crystalline reflections in the SAED patterns of the 10% Sr^{2+} and 50% Sr^{2+} nanotubes confirms their amorphous character depicted by XRD.

3.2 Nanoscale Analysis by Electron Energy Loss Spectromicroscopy (EELS)

The chemical composition of the nanotubes was investigated with nanometric resolution by EELS. STEM-EELS offers the advantage of spatial resolution and has been used as powerful technique in biomineralization and biomaterials investigations.

The spectra in Figure 4a exhibit the Sr-L (ca. 1950 eV) and P-K (ca. 2150 eV) edges averaged over typically 100 nm x 100 nm surface area. The Sr/P intensities drastically change as Ca^{2+} is substituted by Sr^{2+} in the samples. Quantifications can be done and typical Sr/P ratios of 0, 0.16, 0.8 and 1.7 are obtained in agreement with the expected composition within the 10% EELS accuracy. The EELS edges at lower energy, also obtained with ca. 100 nm of spatial resolution, are displayed in Figure 4b. A clear change of Ca L (ca. 350 eV) intensity is observed as the amount of Sr^{2+} increases in the samples. On the other hand, the P-L and Sr-M edges are overlapping giving a cumbersome situation where no reliable quantification can be done. STEM-EELS were also done with nanometer scale resolution by acquiring spectromicroscopic images or lines across the apparent walls of the hollow structures (Figure 4c). To achieve such spatial resolution, electron doses have to be increased and the overall SNR ratios of the EELS signal get lower. With such conditions, no quantifications have been done, even for the non-overlapping edges. We focus on the 50% Sr^{2+} amorphous nanotubes where heterogeneities have been robustly measured, notably on the sidewall of the tube. The analysis of Sr-L and P-K edges indicated that the outer surface of the tube (the surface that grows at the interface with the pore) is phosphorus enriched (Figure 4d). With the lower energy edges (figure 4e), it is not possible to differentiate between P and Sr, but comparing with the Ca-L distribution, heterogeneities are present throughout the tube wall. The Sr and Ca distribution do not have maximum intensity at

1   the same position and, in particular a clearer Ca enriched layer at the inner surface of

2   the tube is observed. Furthermore, both surfaces show the presence of additional C-

3   layers. Such carbon layers are often present in STEM-EELS experiments and might be

4   due to contamination during the STEM experiments or the sample preparation.

5   Additional EELS experiments have been done keeping the sample near LN_2

6   temperature, that is known to strongly reduce contamination and degradation issues, and

7   similar carbon rich layers of several nm have been detected in the outer surface (Figure

8   S7). The presence of carbonate groups can be observed by EELS since its spectroscopic

9   C-K fine structure is different from the one of amorphous carbon (or contamination

10   carbon or heavily damage organic carbon). As shown in Figure S7d, carbonate ions are

11   present in the Sr(ACP), and at the Ca enriched layer at the inner surface. On the other

12   hand, the carbon layer on the outer surface has a broader spectroscopic structure and

13   might be the beam damaged PAA. These STEM-EELS results clearly evidence

14   heterogeneities from the outer to the inner part of the hollow tubes whose might origin

15   from the precipitation into confined mesoporous cavity.
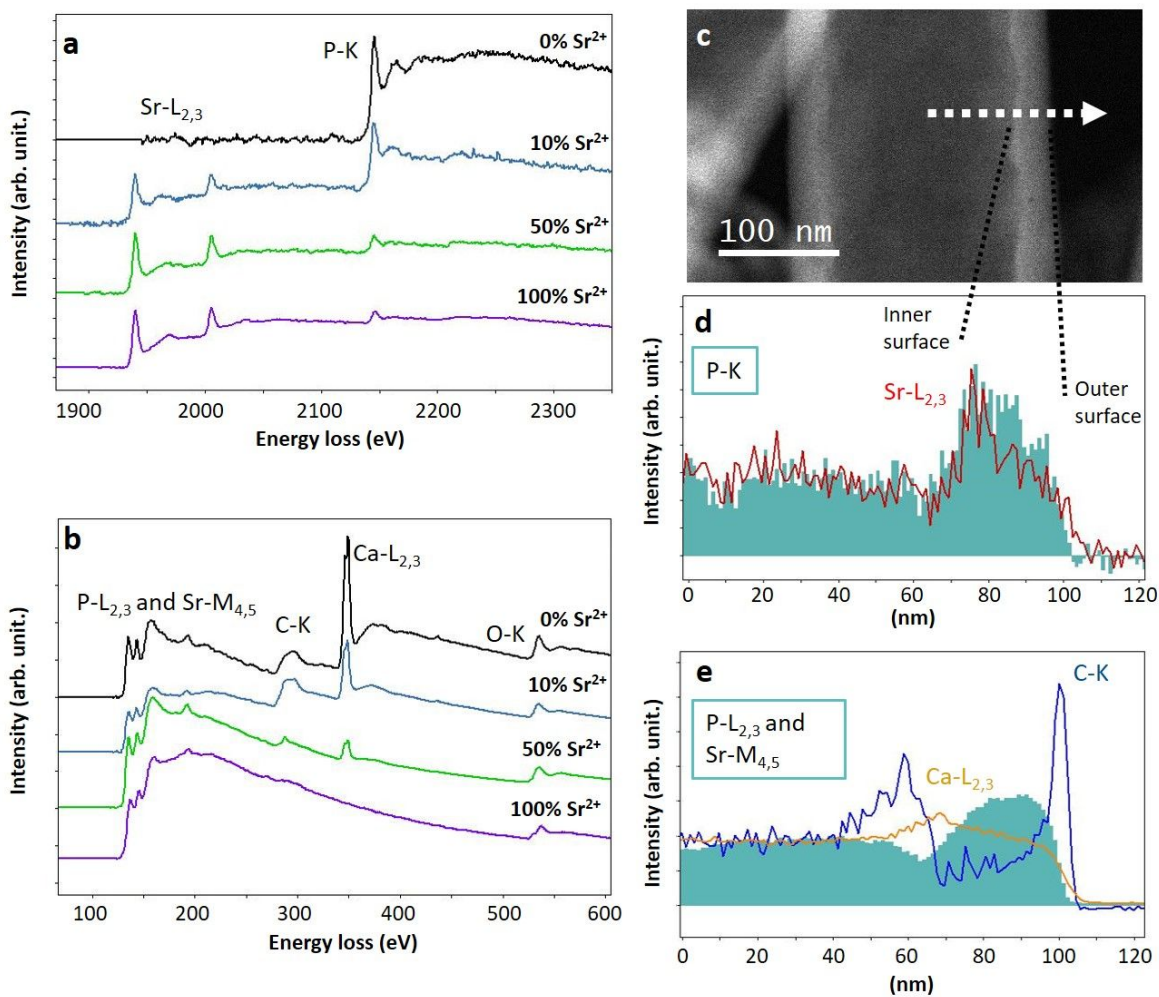
16

1
2
3   1
4
5
6
7
8
9
10
11
12
13
14
15
16
17
18
19
20
21
22
23
24
25
26
27
28
29
30
31
32
33
34
35
36   2
37
38   3 **Figure 4.** (a,b) EELS spectra of the tubes containing 0%Sr^{2+}, 10%Sr^{2+}, 50%Sr^{2+} and 100%Sr^{2+}.
39
40   4 (c,d,e) EELS spectromicroscopy performed on the 50%Sr^{2+} nanotube showing the presence of
41   5 several compositional heterogeneities.
42
43
44
45
46
47
48
49
50
51
52
53
54
55
56
57
58
59
60

1

3.3 Formation mechanism of Sr(CaP) nanotubes

From these results it can be clearly seen that Sr^{2+} and physical confinement have a marked effect over the formation CaP particles in terms of size, morphology, and selection of mineral phase. For instance, while the most reported morphology of ACP is spherical, here we were able to tailor the shape of Sr(ACP) into tubes thanks to the boundary offered by the membrane pores which in turn direct the mineral growth.[32] Likewise, the nanometric apatite crystals precipitated in absence of Sr^{2+} assembled into tubes, rather than the usually spherulitic morphology.[31] Interestingly, while collagen is reported to define the structural features of bone mineral, biomimetic apatite was formed here only by using physical confinement.

Recently, we have shown that the biomimetic precipitation of Sr(ACP) in homogeneous media starts when the degree of Ca^{2+} substitution by Sr^{2+} reaches 25% in the crystalline lattice of apatite.[32] However, this amorphous phase was stabilized in the reaction medium only at higher degrees of Sr^{2+} substitution, namely 50 and 75%. Here, by controlling the physical environment where the precipitation takes place, Sr(ACP) was formed at lower amounts of Sr^{2+} , *i.e.* 10% Sr^{2+}, that is the maximum percentage of this ion found in the bone tissue.[35] EDX analysis confirmed that this effect was provided by the physical confinement since the amount of Sr^{2+} incorporated into the products formed in bulk and within the pores of the membranes was similar. Relying on the pathway of apatite formation *in vitro* and previous findings, we hypothesize that Sr^{2+} acts as kinetic stabilizing agent of ACP during apatite formation.[36,37] As previous reported, one hypothesis is that the confinement provided by the membrane pore reduces the contact of the particles with the solution thus hindering redissolution and reprecipitation processes towards crystallization.[38] Actually, the study of the lifetime of

1   different amorphous minerals within limited volumes revealed several mechanisms by

2   which confinement may affect the kinetics of precipitation, including slower transport

3   of ions and reduced convection.[39–41] In any case, the role of confinement is made clear

4   by the presence of nanoscale heterogeneities from the outer to the inner surfaces of the

5   tubes, some of the possible origin being the slower transport of ions, and preferential

6   local dissolution and precipitation.

7   The stabilization of Sr(ACP) in confinement at Sr^{2+} content close to that found

8   in the tissue of animals raises interesting questions concerning its impacts on bone

9   biomineralization. Previous observations have pointed out that ACP infiltrates within

10   the confines of the gap zone in collagen to form bone mineral.[42,43] Notably, higher Sr^{2+}

11   concentrations are found in young bone which is reported to be less crystalline as

12   compared to the long term bone.[44,45] On account of that, our results bring the notion that

13   Sr^{2+} impacts on the early stages of bone mineralization as proposed for Zn^{2+} and non-

14   collagenous proteins.[46,47] Therefore, the role of Sr^{2+} on bone apatite may be further than

15   a simple hetero-ionic exchange with Ca^{2+} or physical adsorption in the mature mineral,

16   as usually described.[48] However, it is important to note that the mineralization *in vitro* is

17   a simplified model of the much more complex biological systems, in which a multitude

18   of specialized molecules and cells are involved in this process.

1

2 ## 3.4. *In vitro* remineralization and Sr^{2+} release evaluation
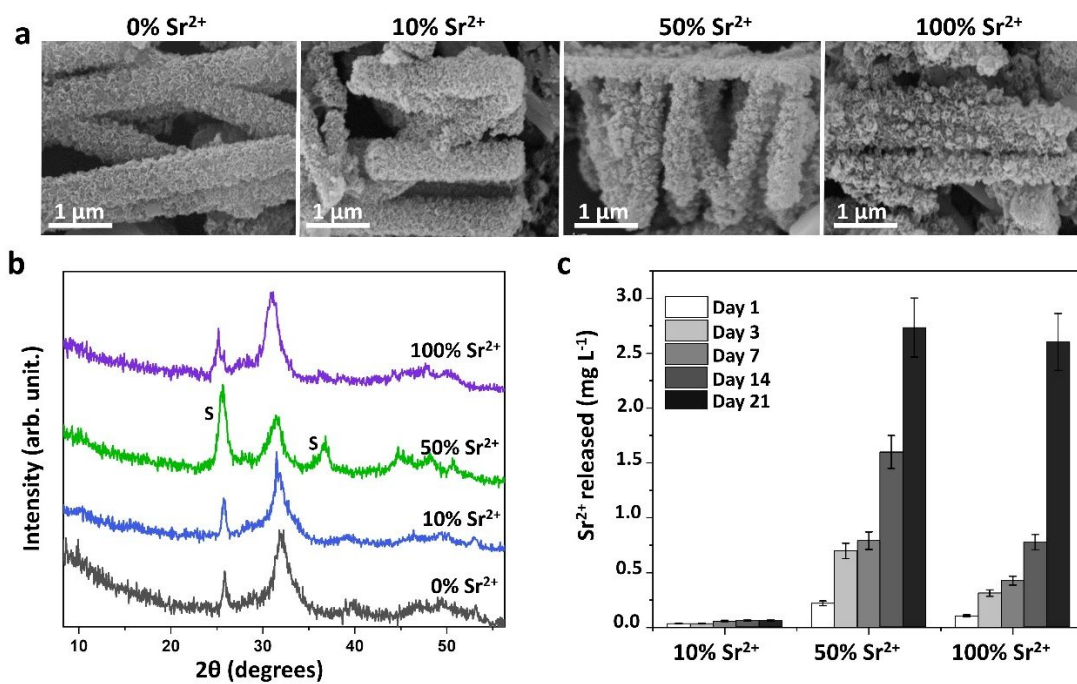
3

4   Aiming at bone tissue regeneration, the bioactivity of the nanotubes was

5 assessed *in vitro* by immersion in SBF, a solution which mimics the blood serum in

6 terms of ionic composition and pH. This is a standard assay to give insights towards the

7 bone forming ability of biomaterials *in vitro* under physiological conditions.[24]

8   XRD revealed that the particles induced the precipitation of biomimetic apatite

9 with typical broad diffraction peaks after 5 days of immersion in SBF (Figure 5b). It

10 should be noted that $SrCO_3$ was formed in addition to apatite in the 50% Sr^{2+} sample, as

11 indicated by the diffraction peaks at $2\theta = 25°$ and $35°$ (indicated by S in the

12 diffractogram). As discussed, this sample is likely formed by a mixture of Sr(ACP) and

13 Sr(ACC). Therefore, in SBF these mineral phases undergo crystallization leading to the

14 formation of apatite and $SrCO_3$. Interestingly, $SrCO_3$ is also a potential biomaterial to

15 osteoporosis treatments, thus, the present experimental conditions and setup could

16 constitute an alternative procedure to precipitate such mixed phases *in vitro*.[33,49]

17   SEM images show that the nanotubes were covered by a newly rough layer

18 formed by nanometric platelets confirming the deposition biomimetic apatite (Figure

19 5a). The fact that the morphology of the nanotubes was maintained, and their diameter

20 increased after the exposure to SBF shows that they acted as template for the nucleation

21 of the new phase, *i.e.* biomimetic apatite. This result also evidenced that the

22 remineralization was spatially controlled, which is important to avoid pathological

23 calcification *in vivo*. It is proposed that Ca^{2+} and PO_4^{3-} from SBF accumulate at the

24 surface of templates leading to the formation of ACP which by redissolution and

25 reprecipitation processes is converted into apatite, the most thermodynamically stable

26 phase of CaP at physiological conditions.[42,36] Then, apatite grows spontaneously by

1   consuming the templating particles and the ions from the medium including Na^+, Mg^{2+}

2   and CO_3^{2-}, evolving towards a bone-like mineral in terms of morphology and

3   composition.[50] The incorporation of Sr^{2+} did not disturb the apatite-forming ability of

4   the tubes during the period of exposure investigated herein, in agreement with previous

5   findings.[51] Hence, these results confirm the potential of these particles to induce

6   biomimetic remineralization in physiological environment.

7   The ability of the particles to release Sr^{2+} in the cell culture medium was

8   evaluated for 1, 3, 7, 14 and 21 days (Figure 5c). The amount of Sr^{2+} increased with the

9   time suggesting the sustained and controlled delivery for long periods. This is an

10   important result as most of the materials are reported to release the total amount of Sr^{2+}

11   within few days. It is noteworthy that the 50% Sr^{2+} sample released higher amount of

12   Sr^{2+} until the 14th day compared to the 100% Sr^{2+} sample. This is likely ascribed to the

13   amorphous nature of the 50% Sr^{2+} sample which may be more soluble than the highly

14   crystalline 100%Sr^{2+} sample. It is worth mentioning that $SrCO_3$ also contributes to the

15   sustained release of Sr^{2+} since in physiological environment this mineral is

16   progressively converted into biomimetic apatite by redissolution and reprecipitation as

17   previously reported.[33] After long periods, the concentrations found in the solutions fall

18   within the Sr^{2+} level in the serum of patients treated with strontium ranelate in which

19   bone healing was achieved in the range of 2–18 mg L^{-1}.[20] These results also show that

20   the composition of the particles can be tailored to release an appropriate level of Sr^{2+}

21   according to the application.

Figure 5. (a) SEM images and (b) X-ray diffraction patterns of the tubes containing different amounts of Sr^{2+} after 5 days of immersion into SBF. The diffractograms were indexed with the hydroxyapatite structure (JCPDS 9-432). The 50% Sr^{2+} sample led to the additional formation of $SrCO_3$ as observed by the additional peaks at $2\theta = 25º$ and $35º$ (indicated by S in the diffractogram). (c) Sr^{2+} released from the 10% Sr^{2+}, 50% Sr^{2+} and 100% Sr^{2+} tubes immersed in the cell culture medium at 37 °C for 12 hours, 1, 3, 7, 14 and 21 days. The amount of Sr^{2+} released by the particles falls in the therapeutic doses used for osteoporosis treatment.

26

3.5. *In vitro* assessment of cytocompatibility of Sr(CaP) nanotubes

It is well-kwon that an imbalance in the activity of osteoblasts and osteoclasts leads to bone diseases, in special osteoporosis. In this sense, the biological response of the particles was assessed *in vitro* by using pre-osteoblastic cells and osteoclasts differentiation protocols.[52]

Confocal microscopy images obtained after 7 days of culture confirm that MC3T3-E1 cells reached confluence displaying a polygonal shape typical from osteoblasts (Figure 6a).[53] SEM images obtained after long term culture (21 days) show that cells remained attached to the substrate with flattened and elongated morphology characteristic of mature osteoblasts (Figure 6b). Moreover, the continuous monolayers of cells indicates that the particles did not disturb their adhesion and proliferation.[54] MTT assays obtained after 21 days of culture confirmed that the particles did not significantly influence MC3T3-E1 viability compared to the control, attesting to their negligibly toxicity towards osteoblasts at the concentration used here, even after long exposure periods (Figure 6c). It has been reported that concentrations of Sr^{2+} close to 17 mg L^{-1} (or higher) are needed to increase the osteoblasts proliferation which is higher than the range investigated herein and found in the plasma of humans treated with strontium ranelate (~10 mg L^{-1}).[55,56] Still, it is important to emphasize that Sr^{2+} may accumulate in the bone tissue provoking pathological calcification.[17,57] Therefore, low doses are preferred in Sr^{2+}-based therapies. In fact, osteoblasts viability is only the initial parameter to be evaluated during mineralization studies.

We further investigated the impacts of the particles on the ALP activity, an important marker of osteogenic activity and therefore bone formation.[58] After 7 days of culture the ALP activity was higher to $10\%Sr^{2+}$ and $50\%Sr^{2+}$ while there were no significative differences between 0% Sr^{2+} and 100% Sr^{2+} compared to the control

27

1   (Figure 6d). ALP activity is an early indicator of osteoblast phenotype differentiation,

2   therefore the increased ALP activity on day 7 for cells cultured in the presence of the

3   10% and 50% Sr^{2+} particles suggests higher osteogenic differentiation as compared to

4   the pure 0% and 100% Sr^{2+} particles. Likewise, a recent investigation reporting on the

5   treatment of osteoblasts with a Sr^{2+}-flavonoid complex revealed that the increased ALP

6   activity in the presence of Sr^{2+} can be associated to the overexpression of the enzyme

7   whereas the cell viability was maintained.[59] Moreover, these results are in line with *in*

8   *vivo* and *in vitro* studies showing that Ca^{2+} and Sr^{2+} mixed may led to an ideal

9   microenvironment where these ions act synergistically to stimulate osteoblast

10 metabolism at the early stages of differentiation.[49,60] Indeed, the synergism between Sr

11 and other elements such Fe and Cu in promoting bone mineral formation has been

12 demonstrated.[61–63] It is noteworthy that the replacement of Ca^{2+} by Sr^{2+} is reported to

13 enhance the degradability of phosphates. In this regard, it has been speculated that Sr^{2+}

14 substitution in apatite might additionally provide an ion-rich environment conducive for

15 osteogenesis. [60,64,66,67]

16   In general, the ALP activity increased after 14 days of culture, as already

17 described for osteoblast-like cells.[26] This strengths the particles ability to support

18 MC3T3-E1 cells evolution towards mature bone-forming osteoblasts. Finally, Alizarin

19 Red S assays revealed that the mineralization of extracellular matrix by osteoblasts was

20 not negatively affected by the presence of the particles (Figure 6e and Figure S8).

21 Although no statistical significance was found between the samples, a tendency of

22 increased mineralization was observed for the 10% Sr^{2+} and 50% Sr^{2+} samples as

23 compared to the control in agreement with ALP results. Overall, the activity of MC3T3-

24 E1 cells was sustained in the presence of the particles strengthening their potential

25 application as platform to induce positive osteoblast responses at low doses.

1   Noteworthy, changes in the ζ-potential values after immersion in the cell culture

2   medium can be assigned to modifications on the particles' surface by adsorption of

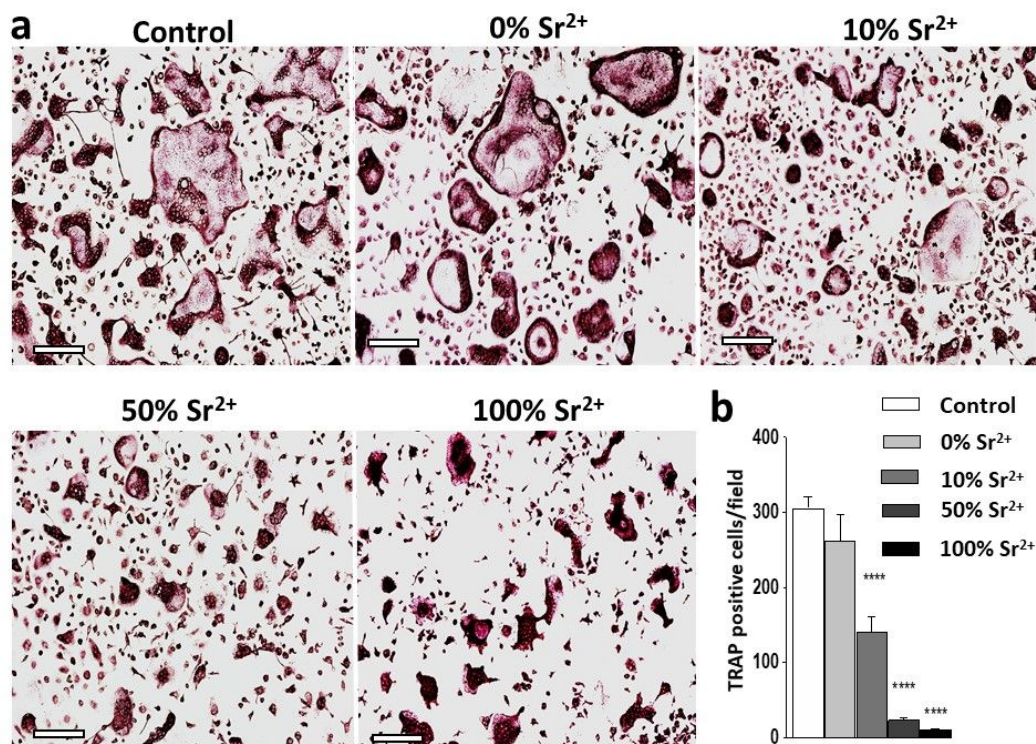3   serum proteins and other components which are known to enhance colloidal stability.[68]
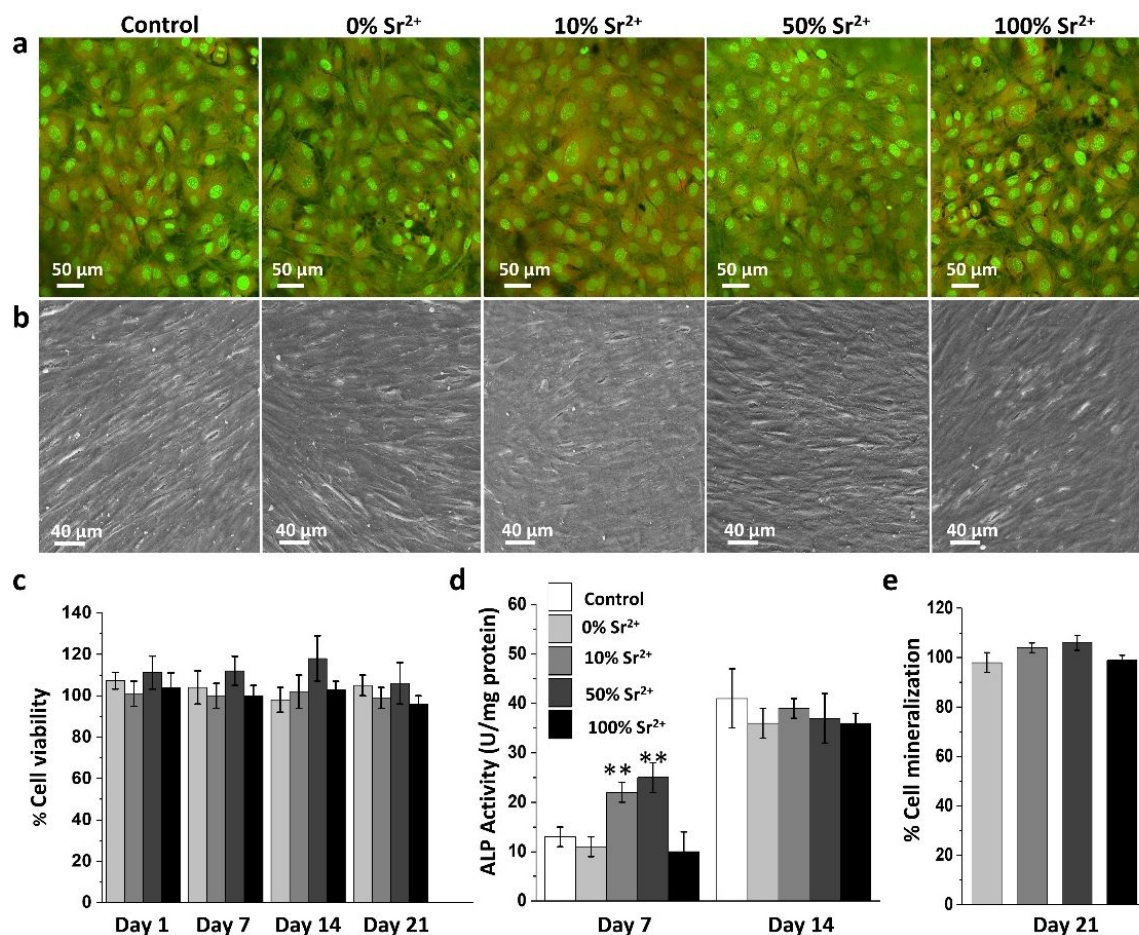
4

Figure 6. (a) Confocal microscopy and (b) SEM images of MC3T3-E1 cells cultured for 7 and 21 days respectively, in the absence (control) and in the presence of Sr(CaP) nanotubes containing 0% Sr^{2+}, 10% Sr^{2+}, 50% Sr^{2+} and 100% Sr^{2+}. (c) Cell viability versus control measured by MTT assay after 24 h, 7, 14 and 21 days of culture, (d) activity of ALP in the osteoblasts' membrane fraction after 7 and 14 days of culture and (e) quantification of mineralized nodules formed in the wells after 21 days of culture. Results represent the mean values ± standard deviation for triplicate determination for each experiment. Multiple statistical comparisons were performed by two-way ANOVA, $**p < 0.01$.

1

2   Next, we evaluated the impact of the particles on osteoclasts differentiation and

3   function. Bone marrow-derived monocytes/macrophages (BMMs) were cultured under

4   osteoclastogenic condition medium in the presence of the 0,10, 50 and 100% Sr^{2+}

5   nanotubes and TRAP staining was performed to identify osteoclasts differentiation. The

6   formation of multinucleated osteoclasts was inhibited by the Sr^{2+} loaded particles

7   whereas no significant differences in relation to the control were found to the 0%Sr^{2+}

8   particles (Figure 7a). Quantitative measurement confirmed that the number of TRAP

9   positive cells was reduced as the Sr^{2+} concentration increased in the particles (Figure

10   7b). To evaluate the ability of the tubes to inhibit bone resorption, osteoclasts were

11   cultured now on hydroxyapatite-coated plates and in the presence of the particles

12   containing different amounts of Sr^{2+}. The formation of demineralization pits was

13   prevented by the Sr^{2+} loaded particles (Figure 8a). Quantification of the areas of the pits

14   confirmed that the demineralization capacity of osteoclasts was significantly reduced by

15   the 10% Sr^{2+} particles or completely inhibited in the case of the 50% Sr^{2+} and 100%

16   Sr^{2+} particles (Figure 8b).

17   Overall, these results are in agreement with previous investigations which

18   demonstrated that Sr^{2+} released from biomaterials and particles inhibit osteoclast

19   differentiation and resorption activities.[69] Nevertheless, Sr^{2+} levels much higher (88 mg

20   L^{-1}) than those found in the serum of patients treated with strontium ranelate (10 mg L^{-1})

21   are usually described for eliciting such anti-osteoclastogenic effects.[70] Herein, a low

22   amount of Sr^{2+} (less than 0.2 mg L^{-1}) was enough to significantly hinder osteoclast

23   activity and differentiation. Interestingly, the % Sr^{2+} incorporated in these particles is in

24   the physiological percentage found in bone tissue (10% mol with respect to Ca^{2+}).[63]

25   Even the highest Sr^{2+} concentration used here (0.7 mg L^{-1}) was lower than that used in

26   other investigations reporting on bioglasses able to delivery Sr^{2+} within the range

1 described as efficient to trigger antiosteoporotic effects *in vivo* (~5 mg L^{-1}).[19] This is an

2 important feature, as the side effects of Sr^{2+} accumulation in bone cannot be overlooked;

3 although high doses decrease differentiation and metabolism of osteoclasts it may also

4 lead to pathological mineralization.[17,17] Actually, the regulation of bone cells

5 metabolism by Sr^{2+} is quite ambiguous. Several studies have demonstrated that

6 osteoblasts response to Sr^{2+} might be a question of optimal environment rather than a

7 concentration driven effect.[49,62]

8   On the basis of our results and the literature presented in this discussion, we

9 believe that tuning the Sr^{2+} and Ca^{2+} concentrations is crucial for the design of materials

10 to bone regeneration and the approach described herein provides an effective way to do

11 this.

12

13

14

15

16

17

18

19

Figure 7. (a) Representative images and (b) quantification of TRAP-positive osteoclasts cultured for 4 days. Bone marrow macrophages (BMMs) was cultured under M-CSF and RANKL stimulation, in the absence (control) and in the presence of the Sr(CaP) tubes containing 0% Sr^{2+}, 10% Sr^{2+}, 50% Sr^{2+} and 100% Sr^{2+}. Results represent the mean value ± standard deviation (n=5) representative of two independent experiments. One-way ANOVA, followed by Tukey's post-test.****$p< 0.001$, compared to control. Scales bars represent 100 μm.
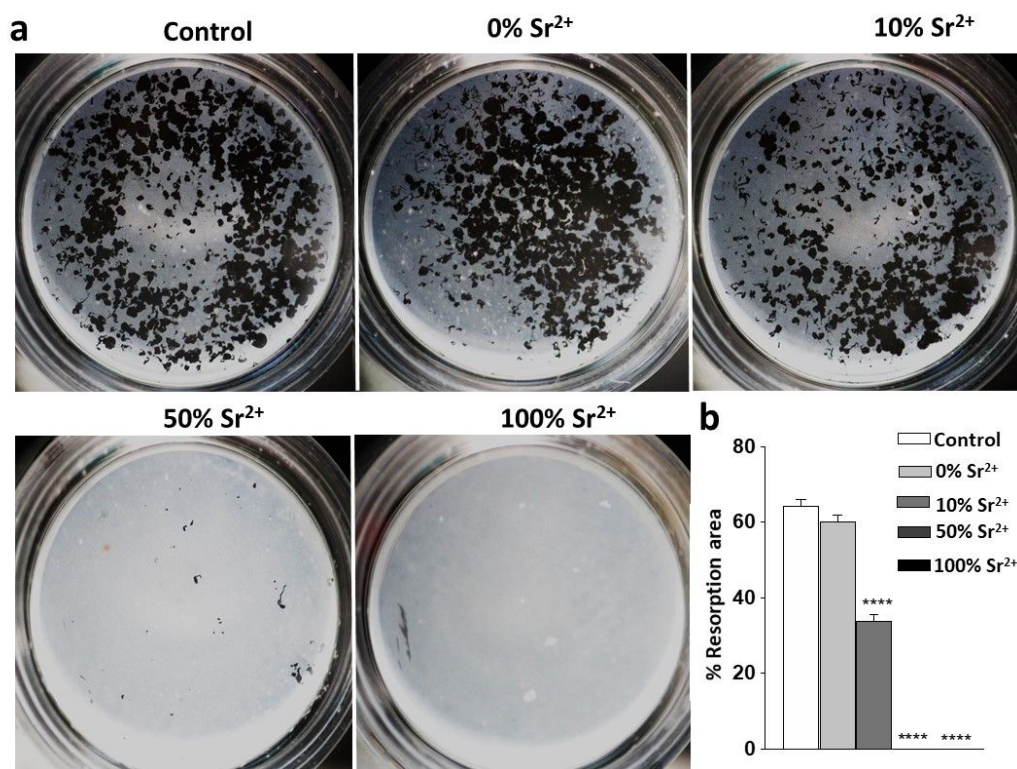
1

2

Figure 8. (a) Representative images and (b) quantification of resorption area induced by osteoclasts cultured in hydroxyapatite-coated plates for 5 days. Bone marrow macrophages (BMMs) was cultured under M-CSF and RANKL in hydroxyapatite-coated plates, in the absence (control) and in the presence of Sr(CaP) tubes containing 0% Sr^{2+}, 10% Sr^{2+}, 50% Sr^{2+} and 100% Sr^{2+}. Results represent the mean value ± standard deviation (n=5) representative of two independent experiments. One-way ANOVA, followed by Tukey's post-test.****$p < 0.001$, compared to control.

4. CONCLUSIONS

A bioinspired approach relying on physical confinement was developed to form Sr(CaP) nanotubes suitable to be used as building blocks of bone. In contrast to previous investigations, biomimetic platelets of apatite were formed here without the need of collagen, thus representing an innovative way to form fibril-like biomimetic biomaterials. The combination of Sr^{2+} and CaP yielded multifunctional particles able to induce osteoblasts proliferation, biomimetic remineralization and to reduce the differentiation and resorption activity of osteoclasts. Moreover, the increased ALP activity found for the $10\%Sr^{2+}$ and $50\%Sr^{2+}$ samples supports their positive effect on the cell maturation and mineralization. Different from the current therapies, all these fundamental aspects for bone regeneration were triggered simultaneously here, and most importantly at low doses of Sr^{2+} which is crucial to avoid its side effects. By showing that Sr^{2+} can be effective at low concentrations when combined with CaPs, this investigation reconciliates the reports of pathological mineralization at excess of Sr^{2+} with its therapeutic effects. Going further, this investigation provides a facile strategy to produce a new generation of biomimetic ceramics with relevant biological responses.

5. ACKNOWLEDGMENTS

6. ASSOCIATED CONTENT

SEM images of the track-etched polycarbonate membrane; SEM images of submicrometer tubes formed using 400 nm pore-size track-etched membranes; Determination by TEM-EDX of the Sr^{2+} content in the particles formed in bulk and confinement; Zeta potential (ζ) versus pH curves obtained for Sr(CaP) nanotubes; ATR-FTIR spectra of Sr(CaP) nanotubes, STEM-HAADF image of 10% Sr^{2+} nanotube; TEM-EDX mapping images of 10% Sr^{2+} and 50% Sr^{2+} nanotubes; STEM-EELS spectra obtained at low temperature by LN_2 sample holder of 50% Sr^{2+} nanotube; Photographs of Alizarin Red S stained osteoblasts´ cultures.

7. REFERENCES

(1)   de Melo Pereira, D.; Habibovic, P. Biomineralization-Inspired Material Design for Bone Regeneration. *Adv. Healthc. Mater.* **2018**, *7* (22), 1–18.

(2)   Reznikov, N.; Bilton, M.; Lari, L.; Stevens, M. M.; Kröger, R. Fractal-like Hierarchical Organization of Bone Begins at the Nanoscale. *Science.* **2018**, *360,* No. eaao2189.

(3)   Liu, J.; Yu, P.; Wang, D.; Chen, Z.; Cui, Q.; Hu, B.; Zhang, D.; Li, Y.; Chu, H.; Li, J. Wood-Derived Hybrid Scaffold with Highly Anisotropic Features on Mechanics and Liquid Transport toward Cell Migration and Alignment. *ACS Appl. Mater. Interfaces* **2020**, *12* (15), 17957–17966.

(4)   Glimcher, M. J. Bone: Nature of the Calcium Phosphate Crystals and Cellular, Structural, and Physical Chemical Mechanisms in Their Formation. *Rev. Mineral. Geochemistry* **2006**, *64* (1), 223–282.

(5)   Habraken, W.; Habibovic, P.; Epple, M.; Bohner, M. Calcium Phosphates in Biomedical Applications: Materials for the Future? *Mater. Today* **2016**, *19* (2), 69–87.

(6)   Weiner, S.; Wagner, H. D. The Material Bone: Structure-Mechanical Function Relations. *Annu. Rev. Mater. Sci.* **1998**, *28* (1), 271–298.

(7)   Pek, Y. S.; Gao, S.; Arshad, M. S. M.; Leck, K. J.; Ying, J. Y. Porous Collagen-Apatite Nanocomposite Foams as Bone Regeneration Scaffolds. *Biomaterials* **2008**, *29* (32), 4300–4305.

(8)   Ramírez-Rodríguez, G. B.; Delgado-López, J. M.; Iafisco, M.; Montesi, M.; Sandri, M.; Sprio, S.; Tampieri, A. Biomimetic Mineralization of Recombinant Collagen Type I Derived Protein to Obtain Hybrid Matrices for Bone Regeneration. *J. Struct. Biol.* **2016**, *196* (2), 138–146.

(9)   Lin, K.; Wu, C.; Chang, J. Advances in Synthesis of Calcium Phosphate Crystals with Controlled Size and Shape. *Acta Biomater.* **2014**, *10* (10), 4071–4102.

(10) Yao, S.; Lin, X.; Xu, Y.; Chen, Y.; Qiu, P.; Shao, C.; Jin, B.; Mu, Z.; Sommerdijk, N. A. J. M.; Tang, R. Osteoporotic Bone Recovery by a Highly Bone-Inductive Calcium Phosphate Polymer-Induced Liquid-Precursor. *Adv. Sci.* **2019**, *6* (19), 1900683.

(11) Yuan, H.; Fernandes, H.; Habibovic, P.; De Boer, J.; Barradas, A. M. C.; De Ruiter, A.; Walsh, W. R.; Van Blitterswijk, C. A.; De Bruijn, J. D. Osteoinductive Ceramics as a Synthetic Alternative to Autologous Bone Grafting. *Proc. Natl. Acad. Sci. U. S. A.* **2010**, *107* (31), 13614–13619.

(12) Marie, P. J. Strontium as Therapy for Osteoporosis. *Curr. Opin. Pharmacol.* **2005**, *5* (6), 633–636.

(13) Bonnelye, E.; Chabadel, A.; Saltel, F.; Jurdic, P. Dual Effect of Strontium Ranelate: Stimulation of Osteoblast Differentiation and Inhibition of Osteoclast Formation and Resorption in Vitro. *Bone* **2008**, *42* (1), 129–138.

(14) Dorozhkin, S. V. Calcium Orthophosphates: Occurrence, Properties, Biomineralization, Pathological Calcification and Biomimetic Applications. *Biomatter* **2011**, *1* (2), 121–164.

(15) Sun, W.; Fan, J.; Wang, S.; Kang, Y.; Du, J.; Peng, X. Biodegradable Drug-Loaded Hydroxyapatite Nanotherapeutic Agent for Targeted Drug Release in Tumors. *ACS Appl. Mater. Interfaces* **2018**, *10* (9), 7832–7840.

(16) Verberckmoes, S. C.; De Broe, M. E.; D'Haese, P. C. Dose-Dependent Effects of Strontium on Osteoblast Function and Mineralization. *Kidney Int.* **2003**, *64* (2), 534–543.

(17) D'Haese, P. C.; Schrooten, I.; Goodman, W. G.; Cabrera, W. E.; Lamberts, L. V.; Elseviers, M. M.; Couttenye, M. M.; De Broe, M. E. Increased Bone Strontium Levels in Hemodialysis Patients with Osteomalacia. *Kidney Int.* **2000**, *57* (3), 1107–1114.

(18) Schrooten, I.; Cabrera, W.; Goodman, W. G.; Dauwe, S.; Lamberts, L. V.; Marynissen, R.; Dorriné, W.; De Broe, M. E.; D'Haese, P. C. Strontium Causes Osteomalacia in Chronic Renal Failure Rats. *Kidney Int.* **1998**, *54* (2), 448–456.

(19) Lao, J.; Jallot, E.; Nedelec, J. M. Strontium-Delivering Glasses with Enhanced Bioactivity: A New Biomaterial for Antiosteoporotic Applications? *Chem. Mater.* **2008**, *20* (15), 4969–4973.

(20) Dahl, S. G.; Allain, P.; Marie, P. J.; Mauras, Y.; Boivin, G.; Ammann, P.; Tsouderos, Y.; Delmas, P. D.; Christiansen, C. Incorporation and Distribution of Strontium in Bone. *Bone* **2001**, *28* (4), 446–453.

(21) Schumacher, M.; Gelinsky, M. Strontium Modified Calcium Phosphate Cements-Approaches towards Targeted Stimulation of Bone Turnover. *J. Mater. Chem. B* **2015**, *4626*, 4626.

(22) Loste, E.; Park, R. J.; Warren, J.; Meldrum, F. C. Precipitation of Calcium Carbonate in Confinement. *Adv. Funct. Mater.* **2004**, *14* (12), 1211–1220.

(23) Kim, Y. Y.; Hetherington, N. B. J.; Noel, E. H.; Kröger, R.; Charnock, J. M.; Christenson, H. K.; Meldrum, F. C. Capillarity Creates Single-Crystal Calcite Nanowires from Amorphous Calcium Carbonate. *Angew. Chemie - Int. Ed.* **2011**, *50* (52), 12572–12577.

(24) Kokubo, T.; Takadama, H. How Useful Is SBF in Predicting in Vivo Bone Bioactivity? *Biomaterials* **2006**, *27* (15), 2907–2915.

(25) Mosmann, T. Rapid Colorimetric Assay for Cellular Growth and Survival: Application to Proliferation and Cytotoxicity Assays. *J. Immunol. Methods* **1983**, *65* (1–2), 55–63.

(26) Simão, A. M. S.; Beloti, M. M.; Rosa, A. L.; de Oliveira, P. T.; Granjeiro, J. M.; Pizauro,

J. M.; Ciancaglini, P. Culture of Osteogenic Cells from Human Alveolar Bone: A Useful Source of Alkaline Phosphatase. *Cell Biol. Int.* **2007**, *31* (11), 1405–1413.

(27)   Hartree, E. F. Determination of Protein: A Modification of the Lowry Method That Gives a Linear Photometric Response. *Anal. Biochem.* **1972**, *48* (2), 422–427.

(28)   Gregory, C. A.; Gunn, W. G.; Peister, A.; Prockop, D. J. An Alizarin Red-Based Assay of Mineralization by Adherent Cells in Culture: Comparison with Cetylpyridinium Chloride Extraction. *Anal. Biochem.* **2004**, *329* (1), 77–84.

(29)   Legeros, R. Z.; Trautz, O. R.; Legeros, J. P.; Klein, E.; Shirra, W. P. Apatite Crystallites: Effects of Carbonate on Morphology. *Science (80-.).* **1967**, *155* (3768), 1409–1411.

(30)   Reznikov, N.; Shahar, R.; Weiner, S. Bone Hierarchical Structure in Three Dimensions. *Acta Biomater.* **2014**, *10* (9), 3815–3826.

(31)   Nassif, N.; Martineau, F.; Syzgantseva, O.; Gobeaux, F.; Willinger, M.; Coradin, T.; Cassaignon, S.; Azaïs, T.; Giraud-Guille, M. M. In Vivo Inspired Conditions to Synthesize Biomimetic Hydroxyapatite. *Chem. Mater.* **2010**, *22* (12), 3653–3663.

(32)   Tovani, C. B.; Gloter, A.; Azaïs, T.; Selmane, M.; Ramos, A. P.; Nassif, N. Formation of Stable Strontium-Rich Amorphous Calcium Phosphate: Possible Effects on Bone Mineral. *Acta Biomater.* **2019**, *92*, 315–324.

(33)   Tovani, C. B.; Oliveira, T. M.; Gloter, A.; Ramos, A. P. Sr2+-Substituted CaCO3Nanorods: Impact on the Structure and Bioactivity. *Cryst. Growth Des.* **2018**, *18* (5), 2932–2940.

(34)   Boskey, A. L. Mineralization of Bones and Teeth. *Elements* **2007**, *3* (6), 385–391.

(35)   Farlay, D.; Boivin, G.; Panczer, G.; Lalande, A.; Meunier, P. J. Long-Term Strontium Ranelate Administration in Monkeys Preserves Characteristics of Bone Mineral Crystals and Degree of Mineralization of Bone. *J. Bone Miner. Res.* **2005**, *20* (9), 1569–1578.

(36)   Wang, X.; Yang, J.; Andrei, C. M.; Soleymani, L.; Grand, K. Biomineralization of Calcium Phosphate Revealed by in Situ Liquid-Phase Electron Microscopy. *Commun. Chem.* **2018**, *1* (1), 80.

(37)   Shih, Y. R. V.; Hwang, Y.; Phadke, A.; Kang, H.; Hwang, N. S.; Caro, E. J.; Nguyen, S.; Siu, M.; Theodorakis, E. A.; Gianneschi, N. C.; Vecchio,K. S.; Chien, S.; Lee, O. K.; Varghese, S. Calcium Phosphate-Bearing Matrices Induce Osteogenic Differentiation of Stem Cells through Adenosine Signaling. *Proc. Natl. Acad. Sci. U. S. A.* **2014**, *111* (3), 990–995.

(38)   Wang, Y. W.; Christenson, H. K.; Meldrum, F. C. Confinement Increases the Lifetimes of Hydroxyapatite Precursors. *Chem. Mater.* **2014**, *26* (20), 5830–5838.

(39)   Meldrum, F. C.; O'Shaughnessy, C. Crystallization in Confinement. *Adv. Mater.* **2020**, 32 (31), *2001068*.

(40)   Ihli, J.; Wang, Y.-W.; Cantaert, B.; Kim, Y.-Y.; Green, D. C.; Bomans, P. H. H.; Sommerdijk, N. A. J. M.; Meldrum, F. C. Precipitation of Amorphous Calcium Oxalate in Aqueous Solution. *Chem. Mater.* **2015**, *27* (11), 3999–4007.

(41)   Anduix-Canto, C.; Kim, Y. Y.; Wang, Y. W.; Kulak, A.; Meldrum, F. C.; Christenson, H. K. Effect of Nanoscale Confinement on the Crystallization of Potassium Ferrocyanide. *Cryst. Growth Des.* **2016**, *16* (9), 5403–5411.

(42)   Lotsari, A.; Rajasekharan, A. K.; Halvarsson, M.; Andersson, M. Transformation of Amorphous Calcium Phosphate to Bone-like Apatite. *Nat. Commun.* **2018**, *9* (1), 4170.

(43)   Akiva, A.; Kerschnitzki, M.; Pinkas, I.; Wagermaier, W.; Yaniv, K.; Fratzl, P.; Addadi, L.; Weiner, S. Mineral Formation in the Larval Zebra Fi Sh Tail Bone Occurs via an Acidic Disordered Calcium Phosphate Phase. *J. Am. Chem. Soc.* **2016**, *138* (43), 14481–14487.

(44)   Li, C.; Paris, O.; Siegel, S.; Roschger, P.; Paschalis, E. P.; Klaushofer, K.; Fratzl, P. Strontium Is Incorporated into Mineral Crystals Only in Newly Formed Bone during Strontium Ranelate Treatment. *J. Bone Miner. Res.* **2010**, *25* (5), 968–975.

(45)   Chamberlain, T.; Handbook, S. E. Infrared Analysis of Rat Bone : Age Dependency Of. *Science.* **1966**, *153* (3743), 1523–1525.

(46)   Cantaert, B.; Beniash, E.; Meldrum, F. C. The Role of Poly(Aspartic Acid) in the Precipitation of Calcium Phosphate in Confinement. *J. Mater. Chem. B* **2013**, *1* (48),

1   6586–6595.

2 (47) Procopio, A.; Malucelli, E.; Pacureanu, A.; Cappadone, C.; Farruggia, G.; Sargenti, A.;
3   Castiglioni, S.; Altamura, D.; Sorrentino, A.; Giannini, C.; Pereiro, E.; Cloetens, P.;
4   Maier, J. A. M., Iotti, S. Chemical Fingerprint of Zn–Hydroxyapatite in the Early Stages
5   of Osteogenic Differentiation. *ACS Cent. Sci.* **2019**, *5* (8), 1449–1460.

6 (48) Frankær, C. G.; Raffalt, A. C.; Stahl, K. Strontium Localization in Bone Tissue Studied
7   by X-Ray Absorption Spectroscopy. *Calcif. Tissue Int.* **2014**, *94* (2), 248–257.

8 (49) Cruz, M. A. E.; Zanatta, M. B. T.; da Veiga, M. A. M. S.; Ciancaglini, P.; Ramos, A. P.
9   Lipid-Mediated Growth of SrCO 3 /CaCO 3 Hybrid Films as Bioactive Coatings for Ti
10   Surfaces. *Mater. Sci. Eng. C* **2019**, *99* (February), 762–769.

11 (50) Kim, H. M.; Himeno, T.; Kokubo, T.; Nakamura, T. Process and Kinetics of Bonelike
12   Apatite Formation on Sintered Hydroxyapatite in a Simulated Body Fluid. *Biomaterials*
13   **2005**, *26* (21), 4366–4373.

14 (51) Leite, Á. J.; Gonçalves, A. I.; Rodrigues, M. T.; Gomes, M. E.; Mano, J. F. Strontium-
15   Doped Bioactive Glass Nanoparticles in Osteogenic Commitment. *ACS Appl. Mater.*
16   *Interfaces* **2018**, *10* (27), 23311–23320.

17 (52) Jilka, R. L. Biology of the Basic Multicellular Unit and the Pathophysiology of
18   Osteoporosis. *Med. Pediatr. Oncol.* **2003**, *41* (3), 182–185.

19 (53) Uggeri, J.; Guizzardi, S.; Scandroglio, R.; Gatti, R. Adhesion of Human Osteoblasts to
20   Titanium: A Morpho-Functional Analysis with Confocal Microscopy. *Micron* **2010**, *41*
21   (3), 210–219.

22 (54) Suphasiriroj, W.; Yotnuengnit, P.; Surarit, R.; Pichyangkura, R. The Fundamental
23   Parameters of Chitosan in Polymer Scaffolds Affecting Osteoblasts (MC3T3-E1). *J.*
24   *Mater. Sci. Mater. Med.* **2009**, *20* (1), 309–320.

25 (55) Bonnelye, E.; Chabadel, A.; Saltel, F.; Jurdic, P. Dual Effect of Strontium Ranelate:
26   Stimulation of Osteoblast Differentiation and Inhibition of Osteoclast Formation and
27   Resorption in Vitro. *Bone* **2008**, *42* (1), 129–138.

28 (56) Meunier, P. J.; Roux, C.; Seeman, E.; Ortolani, S.; Badurski, J. E.; Spector, T. D.;
29   Cannata, J.; Balogh, A.; Lemmel, E. M.; Pors-Nielsen, S.; Rizzoli, R.; Genant, H. K.;
30   Reginster, J.Y. The Effects of Strontium Ranelate on the Risk of Vertebral Fracture in
31   Women with Postmenopausal Osteoporosis. *N. Engl. J. Med.* **2004**, *350* (5), 459–468.

32 (57) Oste, L.; Bervoets, A. R.; Behets, G. J.; Dams, G.; Marijnissen, R. L.; Geryl, H.;
33   Lamberts, L. V.; Verberckmoes, S. C.; Van Hoof, V. O.; De Broe, M. E.; D'Haese, P. C.
34   Time-Evolution and Reversibility of Strontium-Induced Osteomalacia in Chronic Renal
35   Failure Rats. *Kidney Int.* **2005**, *67* (3), 920–930.

36 (58) Sifert, R. S. The Role of Alkaline Phosphatase in Osteogenesis. *J. Exp. Med.* **1951**, *93*
37   (5), 415–426.

38 (59) Cruz, M. A. E.; Tovani, C. B.; Favarin, B. Z.; Soares, M. P. R.; Fukada, S. Y.;
39   Ciancaglini, P.; Ramos, A. P. Synthesis of Sr-Morin Complex and Its: In Vitro
40   Response: Decrease in Osteoclast Differentiation While Sustaining Osteoblast
41   Mineralization Ability. *J. Mater. Chem. B* **2019**, *7* (5), 823–829.

42 (60) Xie, H.; Gu, Z.; He, Y.; Xu, J.; Xu, C.; Li, L.; Ye, Q. Microenvironment Construction of
43   Strontium-Calcium-Based Biomaterials for Bone Tissue Regeneration: The Equilibrium
44   Effect of Calcium to Strontium. *J. Mater. Chem. B* **2018**, *6* (15), 2332–2339.

45 (61) Li, K.; Dai, F.; Yan, T.; Xue, Y.; Zhang, L.; Han, Y. Magnetic Silicium Hydroxyapatite
46   Nanorods for Enhancing Osteoblast Response in Vitro and Biointegration in Vivo. *ACS*
47   *Biomater. Sci. Eng.* **2019**, *5*, 2208–2221.

48 (62) Basu, S.; Ghosh, A.; Barui, A.; Basu, B. (Fe/Sr) Codoped Biphasic Calcium Phosphate
49   with Tailored Osteoblast Cell Functionality. *ACS Biomater. Sci. Eng.* **2018**, *4* (3), 857–
50   871.

51 (63) Weng, L.; Boda, S. K.; Teusink, M. J.; Shuler, F. D.; Li, X.; Xie, J. Binary Doping of
52   Strontium and Copper Enhancing Osteogenesis and Angiogenesis of Bioactive Glass
53   Nanofibers While Suppressing Osteoclast Activity. *ACS Appl. Mater. Interfaces* **2017**, *9*
54   (29), 24484–24496.

55 (64) Boda, S. K.; Thrivikraman, G.; Panigrahy, B.; Sarma, D. D.; Basu, B. Competing Roles
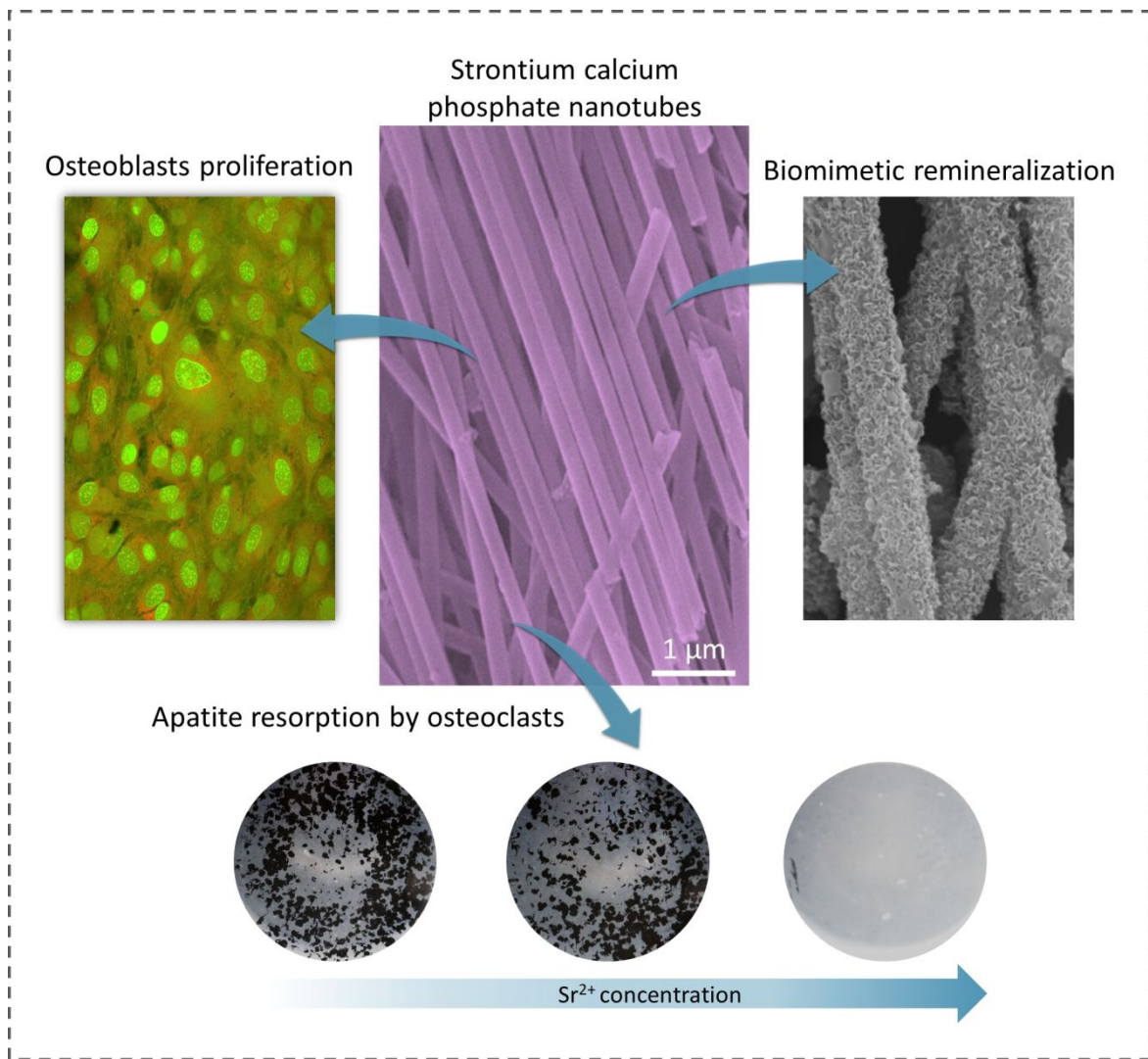
1   of Substrate Composition, Microstructure, and Sustained Strontium Release in Directing
2   Osteogenic Differentiation of HMSCs. *ACS Appl. Mater. Interfaces* **2017**, *9* (23),
3   19389–19408.
4   (65) Deng, Y.; Liu, M.; Chen, X.; Wang, M.; Li, X.; Xiao, Y.; Zhang, X. Enhanced
5   Osteoinductivity of Porous Biphasic Calcium Phosphate Ceramic Beads with High
6   Content of Strontium-Incorporated Calcium-Deficient Hydroxyapatite. *J. Mater. Chem.*
7   *B* **2018**, *6* (41), 6572–6584.
8   (66) Cai, X.; Han, B.; Liu, Y.; Tian, F.; Liang, F.; Wang, X. Chlorhexidine-Loaded
9   Amorphous Calcium Phosphate Nanoparticles for Inhibiting Degradation and Inducing
10   Mineralization of Type i Collagen. *ACS Appl. Mater. Interfaces* **2017**, *9* (15), 12949–
11   12958.
12 (67) Yu, W.; Sun, T. W.; Qi, C.; Ding, Z.; Zhao, H.; Chen, F.; Chen, D.; Zhu, Y. J.; Shi, Z.;
13   He, Y. Strontium-Doped Amorphous Calcium Phosphate Porous Microspheres
14   Synthesized through a Microwave-Hydrothermal Method Using Fructose 1,6-
15   Bisphosphate as an Organic Phosphorus Source: Application in Drug Delivery and
16   Enhanced Bone Regeneration. *ACS Appl. Mater. Interfaces* **2017**, *9* (4), 3306–3317.
17 (68) Ribeiro, A. R.; Gemini-Piperni, S.; Travassos, R.; Lemgruber, L.; Silva, R. C.; Rossi, A.
18   L.; Farina, M.; Anselme, K.; Shokuhfar, T.; Shahbazian-Yassar, R.; Borojevic, R.;
19   Rocha, L.A.; Werckmann, J.; Granjeiro J.M. Trojan-Like Internalization of Anatase
20   Titanium Dioxide Nanoparticles by Human Osteoblast Cells. *Sci. Rep.* **2016**, *6* (3), 1–11.
21 (69) Capuccini, C.; Torricelli, P.; Sima, F.; Boanini, E.; Ristoscu, C.; Bracci, B.; Socol, G.;
22   Fini, M.; Mihailescu, I. N.; Bigi, A. Strontium-Substituted Hydroxyapatite Coatings
23   Synthesized by Pulsed-Laser Deposition: In Vitro Osteoblast and Osteoclast Response.
24   *Acta Biomater.* **2008**, *4* (6), 1885–1893.
25 (70) Gentleman, E.; Fredholm, Y. C.; Jell, G.; Lotfibakhshaiesh, N.; O'Donnell, M. D.; Hill,
26   R. G.; Stevens, M. M. The Effects of Strontium-Substituted Bioactive Glasses on
27   Osteoblasts and Osteoclasts in Vitro. *Biomaterials* **2010**, *31* (14), 3949–3956.

1
2
3
4
5
6
7
8
9
10
11
12
13
14
15
16
17
18
19
20
21
22
23
24
25
26
27
28
29
30
31
32
33
34
35
36
37
38
39
40
41
42
43
44
45
46
47
48
49
50
51
52
53
54
55
56
57
58
59
60

1
2
3
4
5
6
7
8
9
10
11
12
13
14
15
16
17
18
19
20
21
22
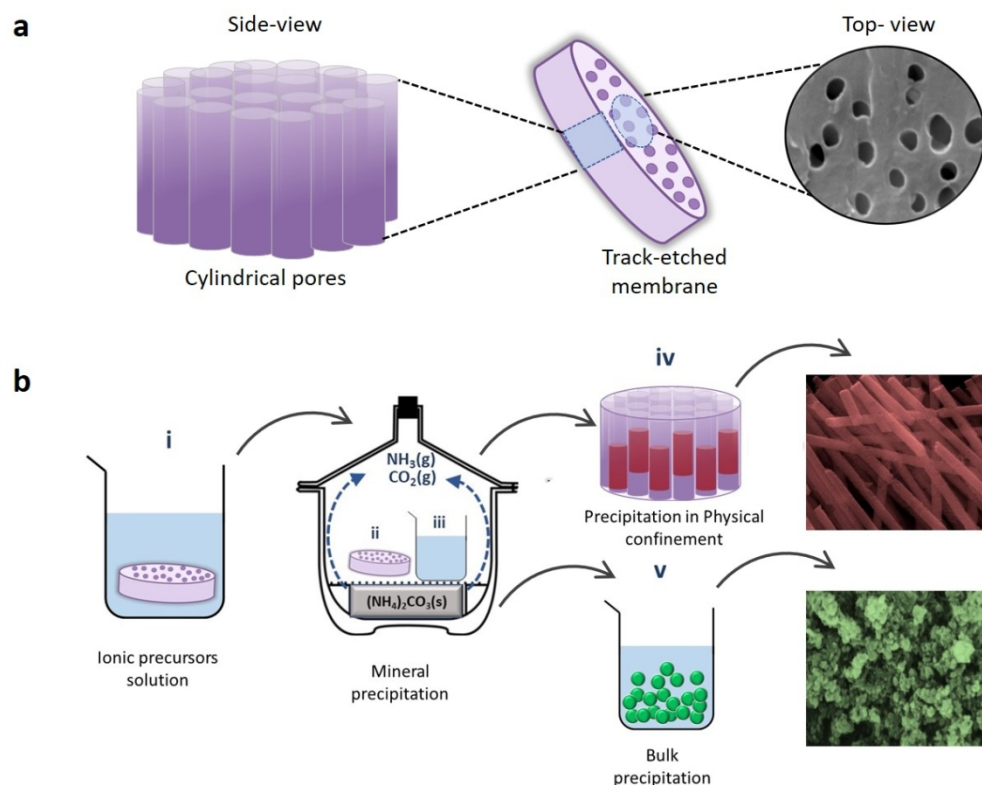23
24
25
26
27

TOC

40

1
2

Figure 1. (a) Schematic representation of a track-etched membrane used as physical confinement to tune the morphology and size of the nanotubes. The side and top view of the membrane shows the cylindrical pores where the precipitation takes place. A SEM image of the surface of a membrane shows the pores. (b) Schematic representation of the precipitation of Sr(CaP) under either physical confinement (i, ii, iv) or in bulk solution (iii and v). The membranes were immersed into the PAA/salt solution for 12 h (i) and then placed in a desiccator containing (NH4)2CO3 (ii) leading to the formation of nanotubes inside the cylindrical pores (iv). The particles (reddish SEM image) were isolated by dissolving the membranes with chloroform followed by centrifugation. A beaker containing the PAA/salt solutions was placed in the desiccator (iii) to conduct the precipitation from bulk solution (v) leading to agglomerated spherical particles (greenish SEM image).
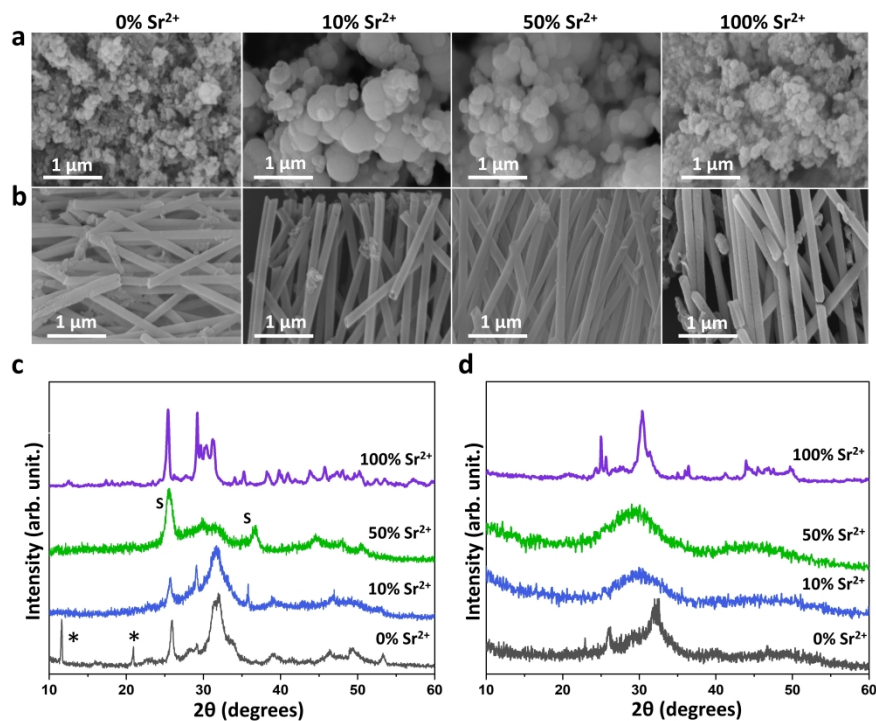
204x167mm (150 x 150 DPI)

Figure 2. SEM images of the phosphate particles formed in bulk solution (a) and in confinement (b). XRD pattern of the particles synthesized in bulk solution (c) and in confinement (d). The products formed in bulk solution were indexed as follows: hydroxyapatite for 0% Sr2+ and 10% Sr 2+ (JCPDS 9-432). The additional peaks (*) observed in the 0% Sr2+ sample may be due to OCP (JPDCS 26–1056). Strontianite (S) (JPDCS 01-071-4899) was found in the 50% Sr2+ sample in addition to an amorphous phase Sr(ACP). Strontium hydrogen phosphate was identified in the 100% Sr2+ sample (JCPDS 23-105026). The samples formed in confinement were identified as hydroxyapatite (0% Sr2+), Sr(ACP) (10% Sr2+ and 50% Sr2+) and strontium hydroxyapatite (100% Sr2+) (JPDCS 33-1348).
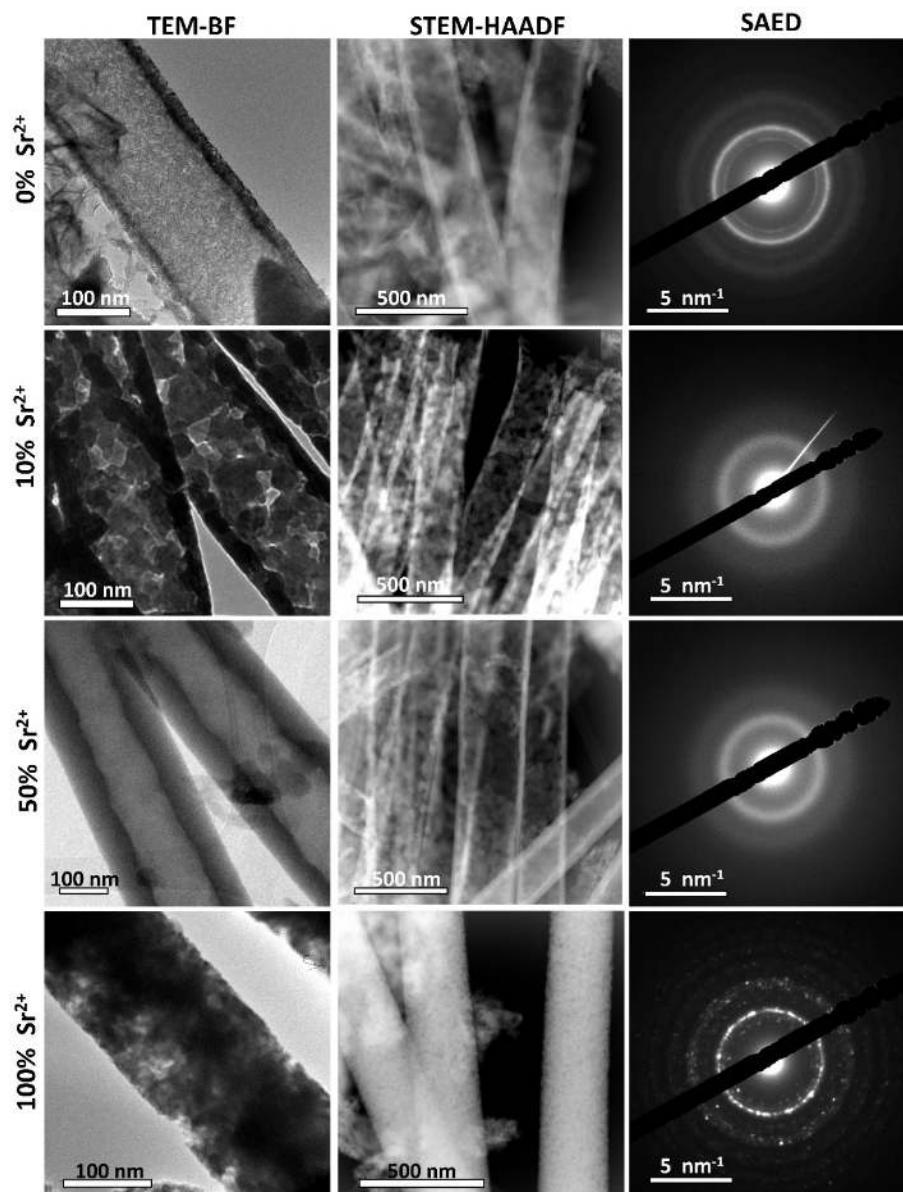
1064x875mm (120 x 120 DPI)

Figure 3.TEM-BF, STEM-HAADF images and SAED patterns of the tubes 0, 10, 50, and 100% Sr2+. STEM-HAADF images show that the 0% Sr2+, 10% Sr2+ and 50% Sr2+ tubes are hollow. The absence of crystalline reflections in the SAED patterns of the 10% Sr2+ and 50% Sr2+ tubes confirms their amorphous character depicted by XRD.
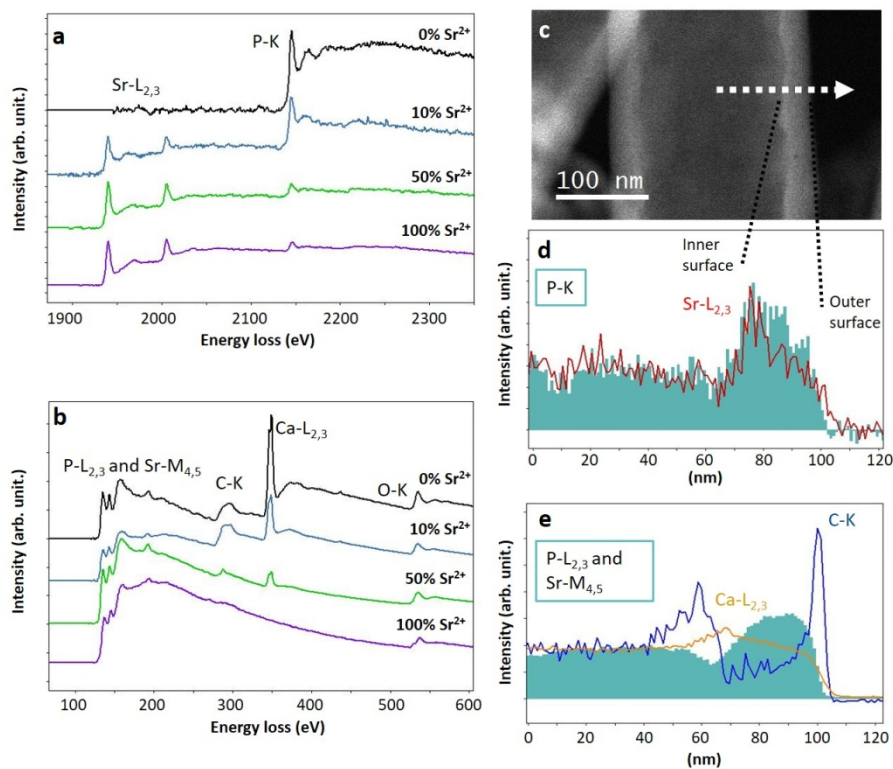
134x176mm (220 x 220 DPI)

Figure 4. (a,b) EELS spectra of the tubes containing 0%Sr2+, 10%Sr2+, 50%Sr2+ and 100%Sr2+ . (c,d,e) EELS spectromicroscopy performed on the 50%Sr2+ tube showing the presence of several compositional heterogeneities.
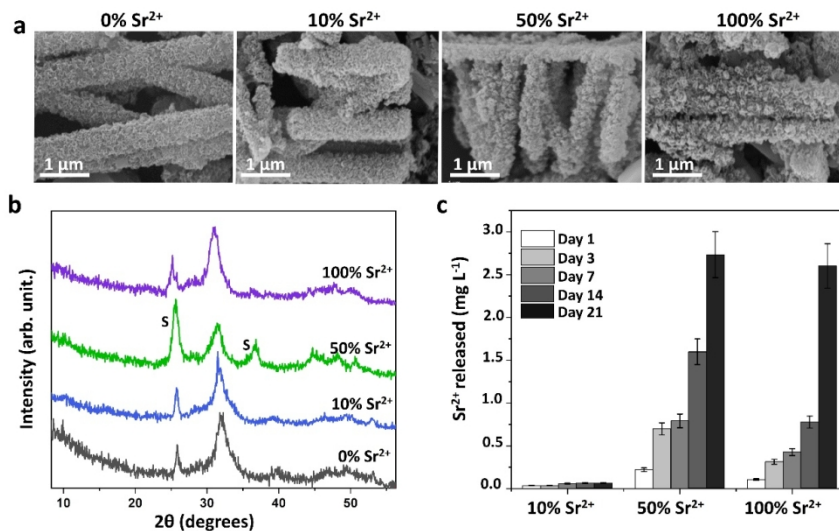
242x188mm (150 x 150 DPI)

Figure 5. (a) SEM images and (b) X-ray diffraction patterns of the tubes containing different amounts of Sr2+ after 5 days of immersion into SBF. The diffractograms were indexed with the hydroxyapatite structure (JCPDS 9-432). The 50% Sr2+ sample led to the additional formation of SrCO3 as observed by the additional peaks at 2θ = 25º and 35º (indicated by S in the diffractogram). (c) Sr2+released from the 10% Sr2+, 50% Sr2+ and 100% Sr2+ tubes immersed in the cell culture medium at 37 °C for 12 hours, 1, 3, 7, 14 and 21 days. The amount of Sr2+ released by the particles falls in the therapeutic doses used for osteoporosis treatment.
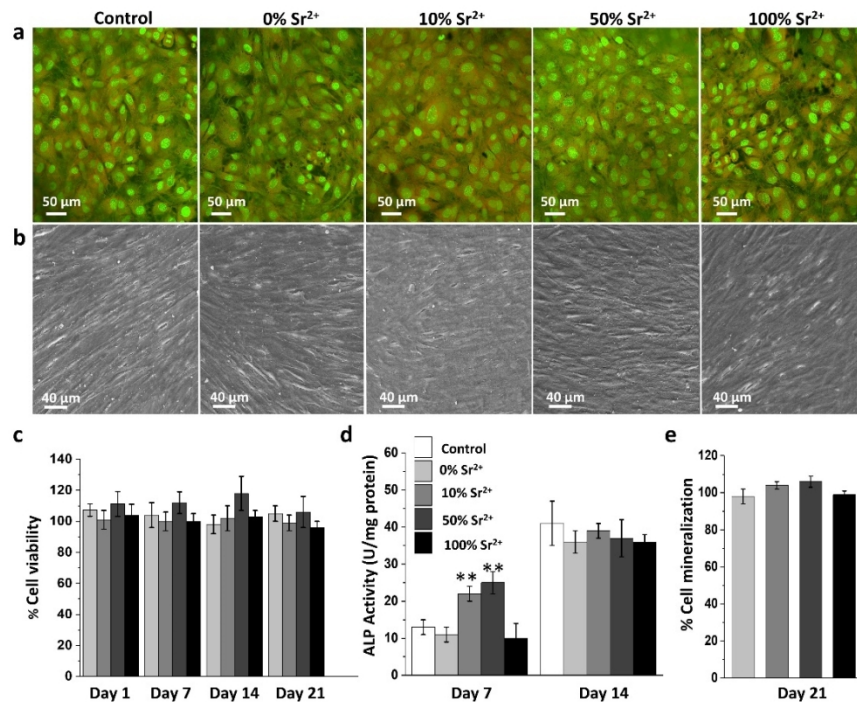
169x96mm (220 x 220 DPI)

Figure 6. (a) Confocal microscopy and (b) SEM images of MC3T3-E1 cells cultured for 7 and 21 days respectively, in the absence (control) and in the presence of Sr(CaP) tubes containing 0% Sr2+, 10% Sr2+, 50% Sr2+ and 100% Sr2+. (c) Cell viability versus control measured by MTT assay after 24 h, 7, 14 and 21 days of culture, (d) activity of ALP in the osteoblasts' membrane fraction after 7 and14 days of culture and (e) quantification of mineralized nodules formed in the wells after 21 days of culture. Results represent the mean values ± standard deviation for triplicate determination for each experiment. Multiple statistical comparisons were performed by two-way ANOVA, **p < 0.01.
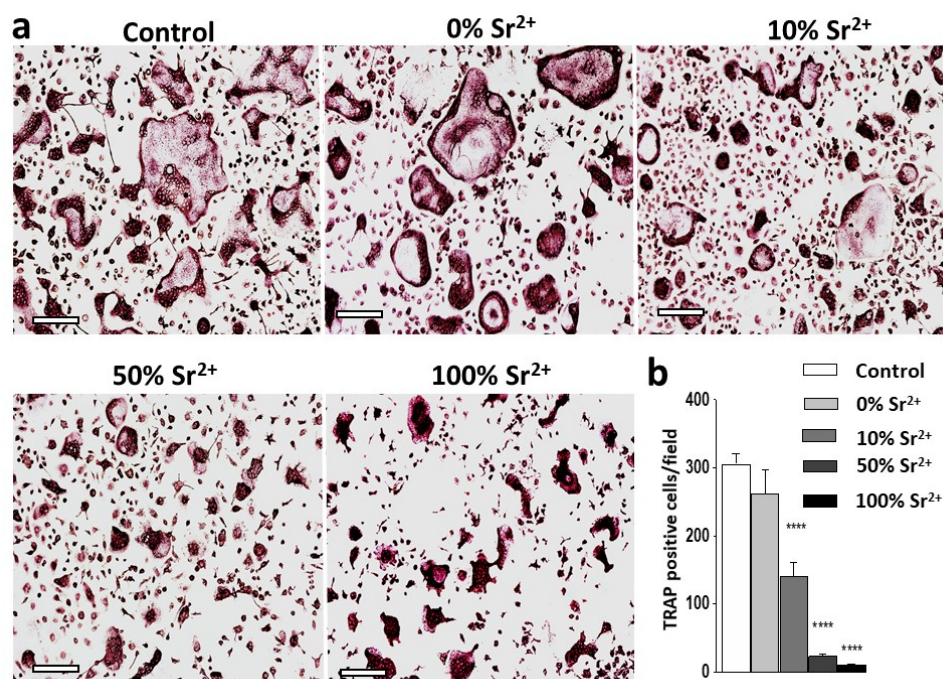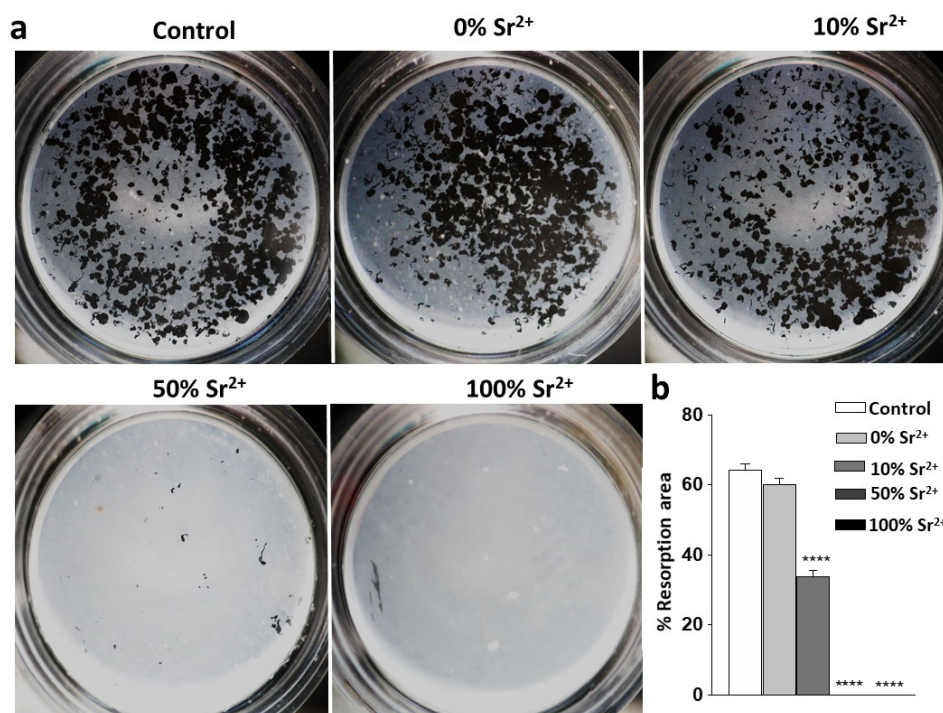
149x112mm (220 x 220 DPI)

Figure 7. (a) Representative images and (b) quantification of TRAP-positive osteoclasts cultured for 4 days. Bone marrow macrophages (BMMs) was cultured under M-CSF and RANKL stimulation, in the absence (control) and in the presence of the Sr(CaP) tubes containing 0% Sr2+, 10% Sr2+, 50% Sr2+ and 100% Sr2+. Results represent the mean value ± standard deviation (n=5) representative of two independent experiments. One-way ANOVA, followed by Tukey's post-test.****p< 0.001, compared to control. Scales bars represent 100 μm.
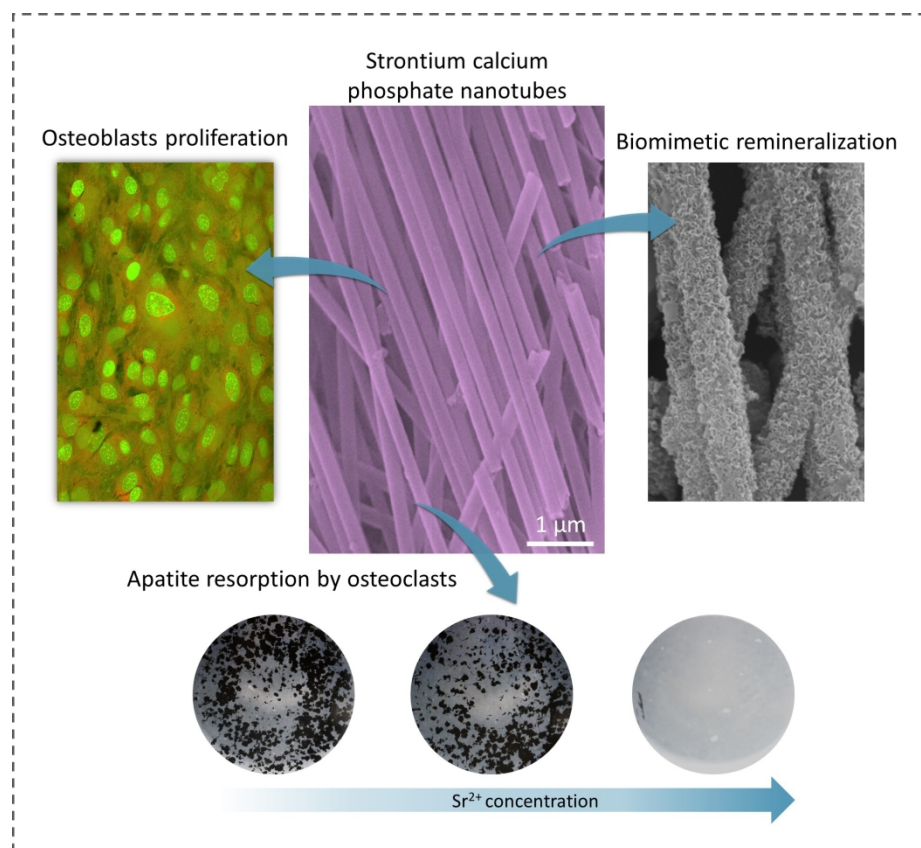
210x152mm (120 x 120 DPI)

1
2
3
4
5
6
7
8
9
10
11
12
13
14
15
16
17
18
19
20
21
22
23
24
25
26
27
28
29
30
31
32
33
34
35
36
37
38
39
40
41
42
43
44
45
46
47
48
49
50
51
52
53
54
55
56
57
58
59
60

Figure 8. (a) Representative images and (b) quantification of resorption area induced by osteoclasts cultured in hydroxyapatite-coated plates for 5 days. Bone marrow macrophages (BMMs) was cultured under M-CSF and RANKL in hydroxyapatite-coated plates, in the absence (control) and in the presence of Sr(CaP) tubes containing 0% Sr2+, 10% Sr2+, 50% Sr2+ and 100% Sr2+. Results represent the mean value ± standard deviation (n=5) representative of two independent experiments. One-way ANOVA, followed by Tukey's post-test.****p< 0.001, compared to control.

234x170mm (120 x 120 DPI)

Osteoblasts proliferation

Strontium calcium phosphate nanotubes

Biomimetic remineralization

1 µm

Apatite resorption by osteoclasts

Sr^{2+} concentration

454x382mm (120 x 120 DPI)